



# Experimental and numerical study on thin silicon wafer CO<sub>2</sub> laser cutting and damage investigation

Kaveh Moghadasi<sup>1</sup> · Khairul Fikri Tamrin<sup>1</sup> · Nadeem Ahmed Sheikh<sup>2</sup> · Abdul Rahman Kram<sup>1</sup> · Pierre Barroy<sup>3</sup> · Fahizan Mahmud<sup>4,5</sup> · Amir Azam Khan<sup>6</sup>

Received: 22 January 2024 / Accepted: 19 April 2024 / Published online: 26 April 2024  
© The Author(s), under exclusive licence to Springer-Verlag London Ltd., part of Springer Nature 2024

## Abstract

This study investigates laser-induced damage in thin silicon (Si) wafer ablation both experimentally and numerically. A 40-W continuous-wave CO<sub>2</sub> laser is employed as the volumetric heat source. Experiments are conducted that involve variations in the laser cutting speed from 5 to 20 mm/s and the number of passes from one to three while maintaining a constant laser power of 40 W for investigation. The measured output parameters include surface morphologies, heat-affected zone (HAZ), and kerf width. For the first time, a finite element solution based on the brittle–ductile transition (BDT) phenomenon is introduced to predict temperature–stress gradients in the laser cutting region. Johnson–Cook (J-C) plasticity, along with the introduced damage criteria, are employed to analyse the cutting characteristics. The results show that the lowest CO<sub>2</sub> laser speed and minimal number of passes enhance Si wafer quality. Nevertheless, increasing cutting speed and the number of passes significantly intensify material ablation and oxidation due to elevated laser heat input. Using optimal parameters, numerical analysis shows a high level of agreement with experimental findings. Transverse/longitudinal stresses correlate with temperature, while the longitudinal stress is substantially lower compared to the transverse stresses due to thermal expansion and the direction of heat transfer. Following that, computed assessments of compressive and tensile stresses are used to refine specific laser parameters and locations for experimental setup.

**Keywords** Laser materials processing · Laser machining · Laser cutting · Laser optical measurement

## 1 Introduction

In electronics, silicon wafers (known as Si wafers) are thin slices of highly pure crystallised silicon (c-Si). The study reported by Atabaki et al. [1] shows that this wafer is a substrate for building electronic devices and circuits at micro-scales owing to its conductivity and affordability. Ultra-thin Si wafers play an important role in fabricating more than 90% of semiconductor devices, as they find their application in electronics and micromechanical devices. As discussed by Jiang et al. [2], it is also a preferred material for use in thermal imaging and night vision applications due to its important optical and biological properties. Drawing from the study done by Arif et al. [3], the escalating surge in demand for microelectronics-driven products during recent years underscores the inescapable necessity of cutting thin silicon wafers for semiconductor manufacturing, which enables customisation, supports testing and quality control, and allows for the creation of specialised configurations devising swift and economically

✉ Khairul Fikri Tamrin  
tkfikri@unimas.my

<sup>1</sup> Faculty of Engineering, Universiti Malaysia Sarawak (UNIMAS), 94300 Kota Samarahan, Sarawak, Malaysia

<sup>2</sup> Department of Mechanical Engineering, Faculty of Engineering, International Islamic University, Islamabad, Pakistan

<sup>3</sup> Laboratoire de Physique de La Matière Condensée, Université de Picardie Jules Verne, Amiens, France

<sup>4</sup> Murata Manufacturing (Sarawak) Sdn. Bhd., Kuching, Sarawak, Malaysia

<sup>5</sup> KT Dynamics Sdn. Bhd., Kuching, Sarawak, Malaysia

<sup>6</sup> School of Chemical and Materials Engineering (SCME), National University of Sciences and Technology (NUST), Islamabad, Pakistan

viable methodologies. Nevertheless, the fine processing of silicon wafer is utterly essential to the industry.

Most semiconductor wafers are brittle materials. Due to the hardness and brittleness of semiconductor wafers, their machining is significantly difficult as compared to conventional mechanical cutting techniques. Using metal or diamond saws, mechanical issues such as irregular path of cut, chip generation, and sharp edges leading to fractures provide intractable challenges for thin Si wafers. For these reasons, ultra-precision machining of Si has become a focused research area in recent years. Over the past many decades, the use of lasers has become popular in material processes such as cutting, joining, welding, and drilling, with advantages such as reduced heat-affected zones (HAZ), higher processing speed, versatile control, and relative environmental friendliness. In addition, the process of cutting using lasers is contact-free, which is particularly useful for Si wafer dicing and cutting. Compared to a mechanical saw, the laser beam allows a micro-scale precision, thereby leading to less chipping and lower delamination. Resultantly, the outcome is a higher yield with a lower cutting width (kerf). So far, different types of laser machines have been utilised by researchers to develop laser cutting of Si wafer.

Li et al. [4] examined femtosecond laser cutting of 200- $\mu\text{m}$ -thick Si wafers by varying pulse energy, parallel scan lines, and cutting speed. It was noted that the increased pulse energy and scan lines improved kerf straightness and reduced sidewall roughness due to Coulomb explosion effects. Mottay et al. [5] demonstrated reduced thermal damage through amplified peak power and shorter interaction times experienced during femtosecond laser processing. Domke et al. [6] observed higher Si ablation rates at slower scanning speeds that plateaued between 100 and 200 mm/s cutting speeds. In another study, Fang et al. [7] employed picosecond lasers for the purpose of cutting polysilicon wafers. They observed an elevation in the surface roughness and the emergence of stress effects. Furthermore, their investigation revealed the presence of numerous micro-cavities, attributed to the subsurface superheating phenomenon. Neuenschwander et al. [8] reported enhanced Si removal using picosecond laser bursts, with higher sub-pulse counts leading to improved energy absorption with increased surface roughness. Metzner et al. [9] found the sub-pulse counts increase ablation efficacy, differing from Neuenschwander et al. [8] due to plasma shielding and redeposition. Shaheen et al. [10] compared lasers' interactions with silicon, observing distinct crater morphologies. Numerical simulations carried out by Cai et al. [11], Zhao et al. [12], Cheng et al. [13], and Cheng et al. [14] focused on crack propagation during laser cutting, including techniques like pre-cracks and guided cleaving. Overall, these studies focused on the effects of processing parameters on crack behaviour in Si

wafer laser cutting, thus contributing towards improved cutting quality and underlying physics.

For laser cutting of Si, a thorough cut is needed along the thickness of the wafer. The main factor is the laser ablation rate, which relates to the wafer diameter as well as its thickness, along with the kerf width and the total time for cutting. Increasing the average laser power to enhance the ablation rate has its own limits. A sufficient amount of laser energy remains one of the cornerstones of effective laser micromachining. Nevertheless, the saturation of the ablation rate owing to higher laser intensity results in thermal and mechanical damages; therefore, the selection of an ideal laser beam cutting speed (feed rate) and number of laser beam passes may improve the total ablation rate and process throughput. On the contrary, although advanced lasers are employed as a non-contact technique to improve the precision during the cutting of silicon, the heat-affected zone cannot be eliminated completely in laser direct processing, which was thoroughly discussed by Wang et al. [15]. Therefore, damage assessment of Si laser cutting is crucial to monitoring the surface quality in order to produce a good surface finish.

It is evident that numerous researchers have employed shorter-wavelength pulsed lasers to cut Si wafers. Compared to the short-wavelength lasers and pulsed lasers, Witteman [16] showed that continuous-wave CO<sub>2</sub> lasers have the capability to deliver a continuous and steady stream of energy. This is due to a consistent and uninterrupted beam, unlike the intermittent energy emitted by short-wavelength lasers and pulsed lasers. This feature is particularly advantageous when precision, uniformity, and minimal thermal damage are required in applications such as cutting, welding, and certain medical procedures. To the best of the authors' knowledge, there is no profound research on the continuous-wave CO<sub>2</sub> laser employed for cutting Si wafer and the corresponding numerical simulation to verify the experimental result and understand the underlying physics. In addition, previous numerical modelling performed by other researchers majorly discussed the crack onset using laser-induced thermal-crack propagation (LITP), employing thermal elastic analysis with the extended finite element method (XFEM). However, material removal from the surface due to strength loss and transition from the Si brittle behaviour to the ductile phase was not considered previously, which necessitates a new detailed mathematical model of thermal-damage propagation and subsequent element deletion based on the definition of material damage characteristics. Therefore, this paper presents the experimental investigation, microstructure evolution, and detailed three-dimensional finite element modelling for the prediction of temperature distributions and thermally driven stresses in the CO<sub>2</sub> laser cutting of Si wafers under various scanning conditions. This approach has the potential to accelerate the development of

optimal manufacturing protocols achieved through effective mathematical and numerical modelling.

The structure of the paper is as follows: Sect. 2 describes the experimental setup, the specimen specifications, and the inspection method along with the employed processing parameters. In Sect. 3, microstructural observations including kerf characteristics, HAZ, surface roughness (Ra), and energy-dispersive X-ray (EDX) analysis, are discussed using digital microscope and scanning electron microscope (SEM) results. In Sect. 4, the numerical simulation of laser material interaction is described through the description of the finite element analysis (FEA) model and associated parameters for simulations. The mathematical model consisting of a volumetric heating source, temperature-dependent material properties, and the brittle-to-ductile transition are included. Section 5 summarises the temperature and stress distributions along with damage/failure propagation profiles. Conclusions are drawn and presented at the end.

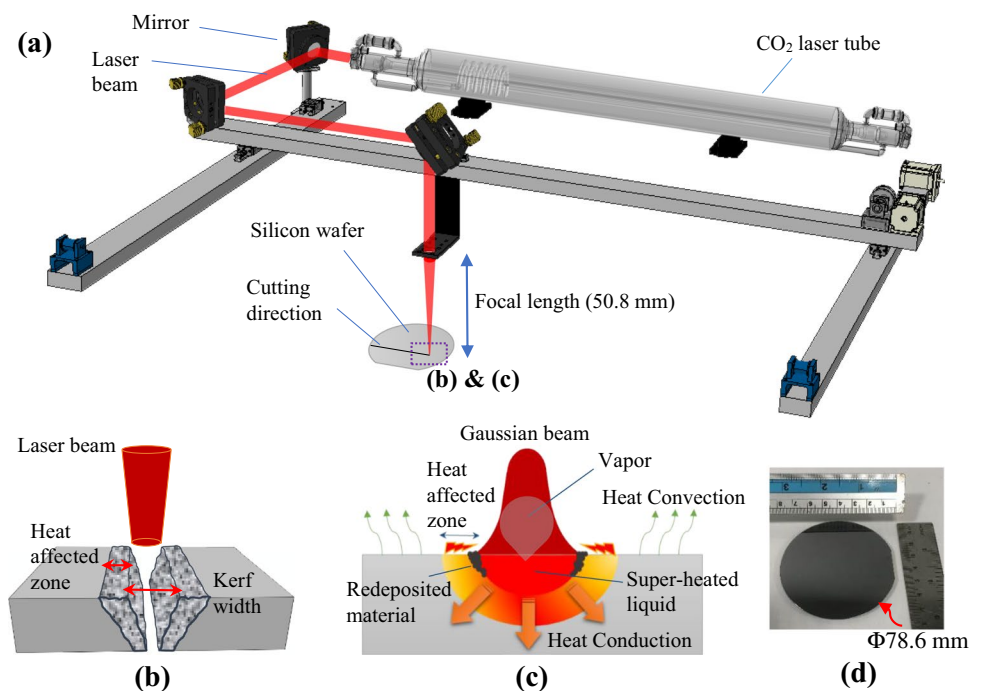
## 2 Experimental setup

### 2.1 Laser cutting system

The experiments on the Si wafer are carried out using a continuous-wave CO<sub>2</sub> laser machining operated in Gaussian mode focused at a focal length of 50.8 mm on the workpiece. The spot size of the laser beam is approximately 200 μm, and the laser wavelength is 10.6 μm. To determine an optimal parameter set for better-cut quality, varying cutting

speeds in the range of 5–20 mm/min and different numbers of laser passes are investigated. The laser power is set to 40 W. The cutting experiments were carried out in a computer numerically controlled Fabool software (Make: smart DIYs Co., Ltd.). The schematics of the operations are shown in Fig. 1a for the CO<sub>2</sub> laser system. The desired motion of the workpiece is achieved by mounting it on the cutting table during laser micro-machining. As the laser ablation mechanism is dominated by thermal effects, however, it takes some time for the imparted heat to penetrate the target (semiconductor) from the source (laser) to subsequently generate a proportionately extensive molten layer. In the findings of Venkatakrishnan et al. [17], it was ascertained that the introduction of assist gas led to a noteworthy reduction (around 30%) in laser cutting speed for thin silicon wafers. Furthermore, the studies conducted by Daud et al. [18] and Tangwarodomnukun et al. [19] revealed contrasting outcomes, suggesting that employing assist gas may not necessarily enhance the cut quality of the machined surface or prevent the silicon from reaching temperatures exceeding its melting point during the laser ablation. Thus, in the current study, both experiments and simulations were performed without activating the assist gas. In the current study, the target material is a single-side polished crystalline silicon wafer of 78.6 mm diameter and 0.35 mm thickness (Fig. 1d). The study done by Huang et al. [20] showed using UV–VIS–NIR spectroscopy measurements that the Si wafer is a very high reflective material. Since the process of material vaporisation generates recoil pressure, which assists in expelling the molten liquid, the objective material is eliminated by

**Fig. 1** Schematic diagram of CO<sub>2</sub> laser machining. **a** Laser setup and specimen cutting direction. **b** Cutting sample by Gaussian laser beam and schematic of material removal mechanisms. **c** Melt expulsion and vaporisation of Si wafer during laser cutting procedure. **d** The utilised silicon wafer in experiments



both the vapour and liquid phases, as shown in Fig. 1c [21]. HAZ denotes a region where alterations in microstructure differentiate between molten and foundational substance materials. This phenomenon finds authentication through a meticulous scrutiny of microstructural manifestations and quantification of defects resulting from laser traversal across the irradiated surface. The vaporised/melted material from the cutting direction is shown as the kerf width. Figure 1b illustrates the schematic diagram of HAZ and kerf width.

## 2.2 Processing parameters and method of characterisation

The quality of the Si wafer-cutting process is influenced by many process variables and parameters. Initial screening of these parameters was carried out to evaluate the operational ranges of each. Amongst all, two important aspects, i.e. number of laser passes ( $N$ ) and laser cutting speed (mm/min) are considered only for reporting here. As shown in previous studies carried out by numerous researchers ([22–25]), a decrease in laser speed increases the laser input energy significantly. It was shown that more gradual laser cutting speeds allow for more controlled material removal, enabling better management of heat accumulation and thermal stresses. This controlled approach minimises the risk of undesirable outcomes such as thermal damage. Since the 10.6- $\mu\text{m}$  CO<sub>2</sub> laser is highly reflected by the Si wafer, this phenomenon becomes a constraint in applying the laser cutting process. A preferred method to enhance the absorptivity of Si is to increase the temperature locally [26, 27]. When the sample's temperature increases, some burnt marks are noticeable, which can be attributed to the formation of a thin oxide layer on the Si surface that may cause irreversible damage (known as optical material damage [28]), subsequently influencing the infrared transmission. Hence, initial preliminary experiments were undertaken to ascertain the requisite laser power for a single laser pass in order to achieve a whole cut. Subsequently, drawing from insights presented in prior investigations concerning single-pass and multi-pass strategies by Oh et al. [29] and Li et al. [30], the approach of this study centres on the selection of lower cutting speeds at the highest laser power setting. Simultaneously, the manipulation of the number of laser passes is employed to amplify the thermal influence at elevated cutting speeds, thereby facilitating the accomplishment of a comprehensive cut. Various levels of these parameters are tabulated in Table 1.

A 3D digital microscope (HIROX RH-2000) was employed to inspect and analyse various objects from laser micromachining of Si wafers at different laser cutting parameters. The kerf width and HAZ were estimated by the captured micrographs. In addition, a SEM (HITACHI TM-3030) was utilised to capture high-resolution images of

**Table 1** The selected laser processing parameters

Specimen	Power (W)	Cutting speed (mm/min)	Number of passes ( $N$ )	Standoff distance (mm)
E1	40	5	1	50.8
E2	40	10	3	50.8
E3	40	20	6	50.8

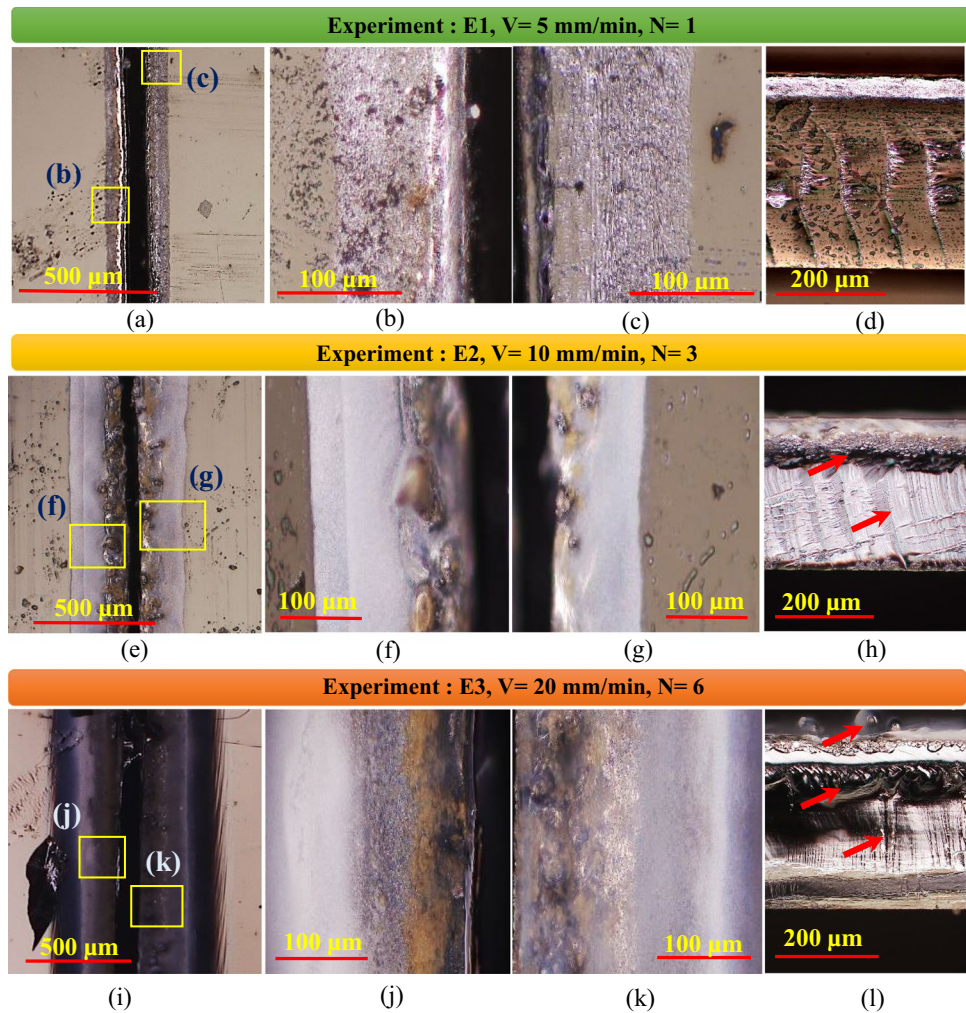
each specimen and measure the geometrical dimensions of irradiation areas in different mediums.

## 3 Results and discussion

### 3.1 Microstructural observations

Figure 2 displays micrographs of cut characteristics taken by a 3D microscope as functions of cutting speed (varying from 5 to 20 mm/s) and number of laser passes (varying from 1 to 6). It is seen from Fig. 2 that the optimum CO<sub>2</sub> laser parameter to achieve a clean surface with no cracks and minimal chippings is set to the minimum cutting speed (5 mm/min) and single laser pass (specimen E1). When the laser at 5 mm/min was used, the laser energy was sufficient to trigger silicon electrons, causing the material to melt and evaporate in the first pass. Figure 2a presents the top surface of the cutting specimen with melted residues. It can be seen that fewer solidified residues appeared on the surface after cutting. On the contrary, as shown in Fig. 2e, i, it is evident that a large portion of the material was ablated from the top surface in specimens E2 and E3, respectively. A higher number of laser passes means higher heat accumulation after each laser pass in the irradiated area, which led to a wider kerf. The laser beam becomes confined within the groove region, leading to an increase in the kerf width through the process of Si melting and vaporisation from the upper surface. Figure 2i shows a significant ablation area on the cut surface of 20 mm/min, which is mainly composed of silicon dioxide. The reason is owing to the significant accumulation of laser heat caused by the higher number of passes. When the number of passes increases, more heat is trapped in the cutting region, thereby inducing material ablation and the oxidation of silicon in the adjacent area. The high intensity of laser energy may improve efficiency in terms of vaporisation through enhanced thermal-material interaction; however, this may also cause oxidation of Si and lead to poor quality of sidewall surfaces. Nevertheless, this may not be of greater concern for full-depth cutting as the sidewalls are ablated in such a scenario with the tendency to shift away from the central focus of the Gaussian laser

**Fig. 2** Optical micrographs of the laser cutting surface of Si wafer using different cutting speeds and number of passes at the same laser power. **a** Specimen E1,  $V=5$  mm/min;  $N=1$ . **b, c** Magnified pictures of heat-affected regions for E1. **d** Cross-sectional macroview of specimen E1. **e** Specimen E2,  $V=10$  mm/min;  $N=3$ . **f, g** Magnified pictures of heat-affected regions for E2. **h** Cross-sectional macroview of specimen E2. **i** Specimen E3,  $V=20$  mm/min;  $N=6$ . **j, k** Magnified pictures of heat-affected regions for E3. **l** Cross-sectional macroview of specimen E3



beam. Similarly, the results indicated by Cheng et al. [13] prove that the degree of ablation rises with the increase of heat input, which would induce severe thermal damage on the sidewall and a dramatic increase in surface roughness.

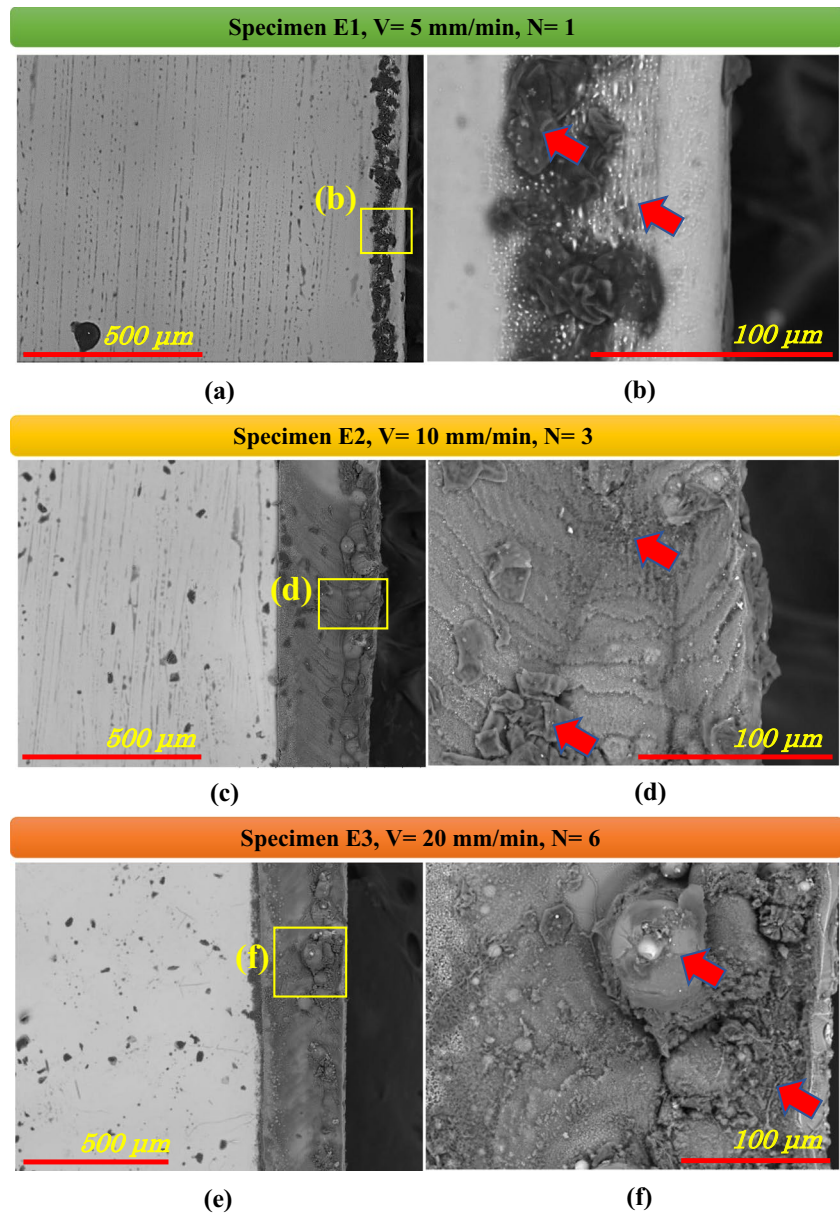
In general, the depth of cut varies inversely with cutting speed; however, a direct proportionality can also be seen for the same with the output power and number of laser passes, as discussed in refs. [31–34]. However, the effect of elliptical beams is also unavoidable, which could produce deeper grooves at optimum laser parameters. This is mainly related to the distribution of laser intensity. In the case of the high level of ellipticity for the elliptic beam spot, one scanning time is assumed to be enough to provide ideal cutting quality. Thus, elliptical distribution is relatively beneficial in terms of improving of the processing efficiency as well as saving overall energy [35–37]. Figure 2b, c contains the magnified pictures of HAZ for experiment E1. In contrast, by increasing the number of passes, the length of HAZ for E2 and E3 becomes notably higher, as shown in Fig. 2f, g, j, k, respectively. With heat conduction, it is noted that a larger degree of ablation is formed along with an enhanced

pile of material debris near the kerf due to excessive heat entering the material.

Figure 2d, h, l shows the cross-section of the cut region. Figure 2h, l shows the formation of distinct peak and valley features along the sidewall for specimens E2 and E3, respectively. In the multi-pass technique (shown in Fig. 2h, l), the quality of the cross-section cut achieved in secondary passes at higher cutting speeds is significantly inferior compared to the cut created by a single pass at lower cutting speeds (Fig. 2d). The most probable reason is related to the existence of HAZ beneath the laser beam, whereby the thermo-physical properties of the affected material is significantly different from pristine silicon.

Figure 3 shows SEM of laser cutting the top surface of the Si wafer at different cutting speeds and number of passes. For laser beam moving at 5 mm/min, Fig. 3a indicates that on the irradiated Si surface, a narrower extent of debris re-deposition in the form of a thin black layer of silica ( $\text{SiO}_2$ ) and carbon oxides was observed (see Fig. 11). Figure 3b (marked red arrows) shows a magnified image of specimen E1, which ascertains a small part of the top surface is

**Fig. 3** SEM morphologies of top cutting surfaces with magnified micrographs for each laser cutting experiment. **a** Specimen E1, 5 mm/min; 1 laser pass. **b** Magnified picture of burnt residues and debris for specimen E1. **c** Specimen E2, 10 mm/min; 3 laser passes. **d** Magnified picture of burnt residues and debris for specimen E2. **e** Specimen E3, 20 mm/min; 6 laser passes. **f** Magnified picture of burnt residues and debris for specimen E3



affected by laser heat and very less debris appeared on the cutting region.

As the cutting velocity was enhanced along with a number of passes, it was observed that the spatter deposition area was getting distributed over larger regions. For E2 and E3, as seen in Fig. 3c, e, respectively, a large amount of material can be seen forming on the top surface during kerf formation after getting melted and subsequent vaporisation. Accordingly, the material solidified adjacent to the cutting zone, which caused the accumulation of melted residues on the top surface and the generation of bigger HAZ. Therefore, more debris deposition was also obtained at a higher number of passes and cutting speed. This can be attributed to the expulsion by recoil pressure from the cut channel after increased molten material generation.

Above the focus position, the laser beam moved through the mirrors, and by passing the focal lens, it was subjected to the Si wafer with no blocking effect. Thereafter, the maximum laser energy was applied to the Si surface to improve the material removal process. As depicted in Fig. 3d, f, specimens E2 and E3 show the formation of irregular shapes and rugged deposition at the surface's top. It is seen (Fig. 3f) that particles of spherical shapes are usually formed in a balling phenomenon as the result of melting and subsequent re-solidification of the ejected droplets. It is seen from the red arrows that the larger molten droplets were found closer to the cut edge and they were solidified adjacent to the cutting region, while smaller debris was deposited further away from the kerf.

The typical behaviour of a homogeneous material follows an approximate log profile, as shown in Fig. 4 for its ablation rate with varying laser fluence (laser energy concentration) at a given wavelength and power of a laser source. The log curve has three distinctive zones. Zone 1 or phase 1 is the pre-ablation region whereby the threshold is yet to reach (i.e., ablation threshold fluence ( $F_{th}$ )). Here, the thermal stresses lead to changes/degradations in the micro-structures in material and its properties upon the impact of laser irradiation, although no ablation occurs. Phase 2 lies between the lower shelf region between  $F_{th}$  and the transition point ( $F_c$ ). This region leads to the activation of Si melting observed in almost all specimens. Here, the ablation rate is relatively low, with better processing quality, a smoother kerf, and less chipping and/or cracking. Thus, better ablation morphology with less debris size and distribution, and HAZ dimension are observed in this phase. The results found in the case of specimen E1 as well as the results of other researchers [38] show good agreement with the observations of phase 2. On the other hand, in phase 3, with the increase in laser fluence, a drastic ablation rate increase is seen at a higher number of passes. A saturated regime is then seen, whereby the processing quality seems to have degraded with less control over the ablation dimensions and generated features. Specimens E2 and E3 demonstrate the results of phase 3.

Figure 5 shows the SEM images of the cross-section of the cut sample performed by the CO<sub>2</sub> laser using different cutting parameters. The magnified pictures for each experiment have been placed to provide a better comparison. These illustrate variations of laser parameters and their effect on the ablation of silicon through the thickness and creation of melted residues and debris on the surface. It is seen from

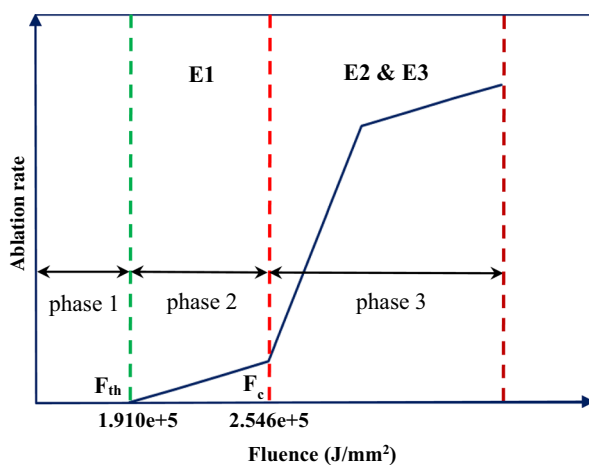


**Fig. 4** Schematic representation of laser ablation rate versus laser fluence for the employed CO<sub>2</sub> laser and homogeneous silicon wafer: laser fluence below ablation threshold fluence ( $F_{th}$ ) corresponds to phase 1, between  $F_{th}$  and transition point ( $F_c$ ) is named as phase 2, and higher than  $F_c$  is considered phase 3

SEM images that melting and ejection of molten material surrounding ablation craters are frequent phenomenon. The density and size of ejected particles vary, however, depending on the value of the cutting speed and the number of laser passes.

The effect of a higher number of passes on the quality of the cutting region was greater than that of the velocity speed. It is seen in Fig. 5a that a lower cutting speed could not only process a neat cutting region but also less slag deposited in the processing zone. Almost no slag is visible adhering to the cutting zone of Si at the cutting speed of 5 mm/min using a single laser pass. This is directly linked to heat transmission and the removal of material. Moreover, the degree of laser scattering can be lowered significantly in a single laser pass, as only debris clusters at the entrance of the cutting region. On the contrary, it is shown in Fig. 5d, g that material slag of large quantities covered the inner zonal walls of the zone of cutting and penetrated throughout the entire depth, which can be attributed to a higher number of passes despite possessing a larger cutting speed value.

It is noteworthy to mention that the appearance of surface striations, as shown in Fig. 5b, e, h, is due to laser heat accumulation in experiments whereby the vapour pressure causes periodic harmonic perturbations in the melt pool, leading to instability under the Gaussian beam profile intensity. This agrees well with the findings of Balbaa et al. [39] and Richter et al. [40].

The ejected particles from craters, which have been produced by the slowest cutting speed and a single laser pass (Fig. 5c), demonstrate less aggregation and agglomeration of particulates on the sample cut surface than that of particles ejected from craters formed by faster cutting speeds and several laser passes, presented in Fig. 5f, i. The cuts introduced by the laser produce molten droplets, which are subsequently solidified at the walls of the cut. As the energy of the laser gets absorbed in the layer of liquidated material beneath the laser pass, this adds to the surface temperature, which can become higher, leading to volume boiling inside the superheated layer. This accumulation and sub-surface boiling/explosions can lead to the ejection of a large number of disintegrated micro-sized droplets. These scattering droplets are then solidified on the wall surface, thus leading to increased roughness values for E2 and E3 ( $R_a = 0.12$  mm and  $R_a = 0.158$  mm, respectively, compared to  $R_a = 0.015$  mm for E1). Resultantly, the scattering re-solidification generates micro-cavities at the surface, which are visible upon removal of the surface layer.

### 3.2 Kerf width and HAZ measurement

The bar graphs in Fig. 6 illustrate that at fixed laser power, increasing the number of passes and cutting speed generates larger kerf widths. This phenomenon is because, at the

**Fig. 5** SEM micrographs of performed experiments using different laser cutting parameters. **a** E1:  $V=5$  mm/min;  $N=1$ . **b, c** Magnified pictures of the cut section for E1. **d** E2:  $V=10$  mm/min;  $N=3$ . **e, f** Magnified pictures of the cut section for E2. **g** E3:  $V=20$  mm/min;  $N=6$ . **e, f** Magnified pictures of the cut section for E3

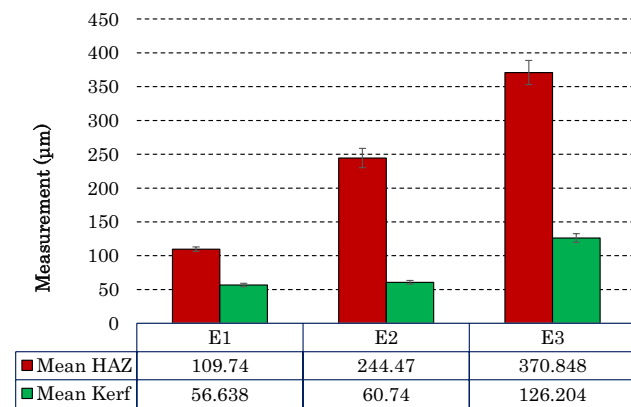
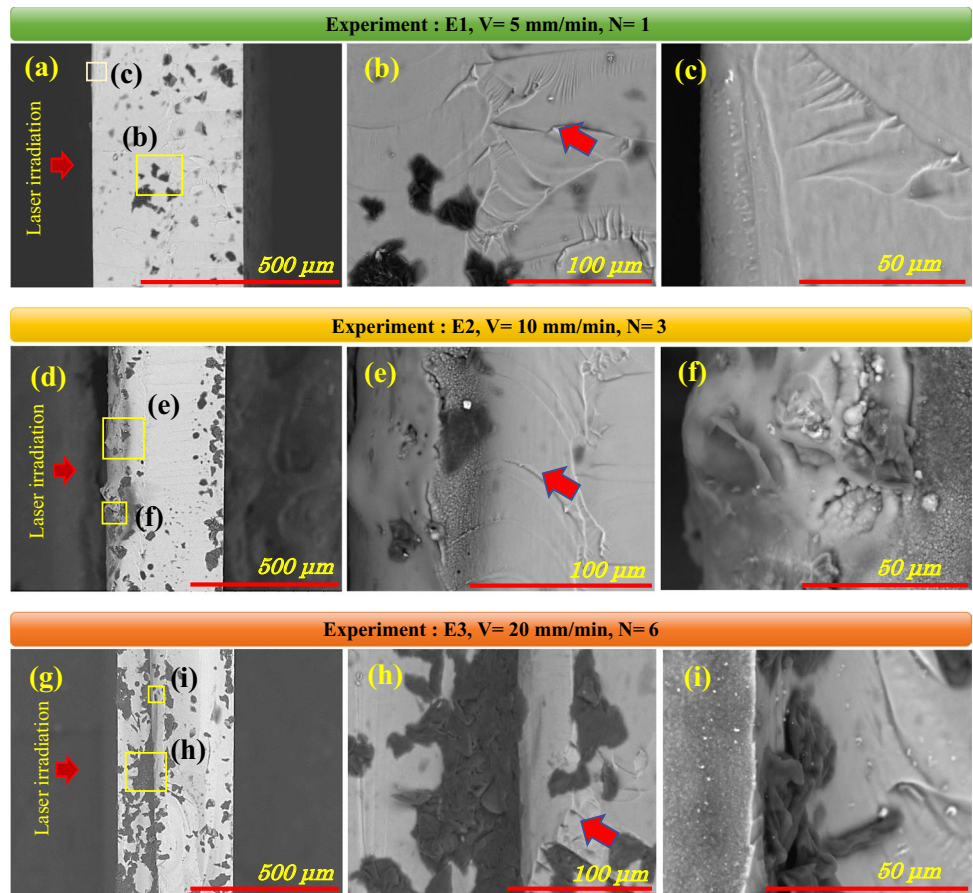


**Fig. 6** The values of mean HAZ and mean kerf width for each laser cutting experiment of Si wafer

beginning of the through cut for experiments E2 and E3, the cutting quality is poor. As elucidated by Soltani et al. [41], a noticeable fraction of laser energy is absorbed by the wall surfaces. Nevertheless, the work of Yeo et al. [42] shows that the absorbed laser energy at the base of the laser cut does not significantly contribute to material ablation. The absorbed laser energy does not effectively contribute

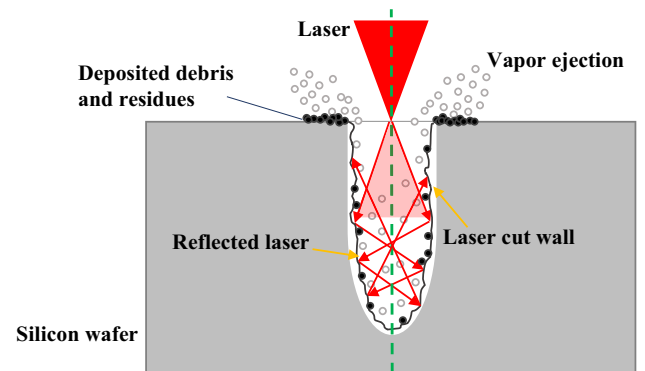


**Fig. 7** Illustration of keyhole form by laser depth cutting and the effect of sidewalls on laser reflection and the creation of a bigger kerf

to the ablation of the material at the base of the laser cut. The rebound of the laser beam off the wall, influenced by the input energy density, plays a distinct role in directing the laser energy to the bottom of the cut, which results in a significant increase in the temperature on the sidewalls, thus melting and burning major part of the specimen (Fig. 7). A similar finding was discussed by other researchers [43, 44]. For each cutting process, a total of five positions for the

kerf width were measured whereby an average kerf width is calculated. Consequently, the error bar would reflect the variation in kerf widths. Similarly, the same method was applied for HAZ measurement.

Figure 7 shows the comparison of focused and reflected laser beam impacts along the central axis of the kerf for a single laser pass cutting as highlighted by a green dotted line. In multi-pass laser cutting, employing higher cutting speed values, the groove width is small in the first laser pass, and the dense generated vapours may block the incident laser beam from penetrating the profound groove to ensure a full-depth cut. Thus, subsequent laser passes are necessitated whereby enlarging the cut area. This increases vapours in the cut groove with ease of ejection in a timely fashion, having a wider spread and enabling the incoming laser beam to penetrate the designated zone. So that the delivery of the laser beam into the lower region is facilitated. Therefore, at a higher cutting speed, the multi-pass technique enhances the efficiency of ablation and makes the full-depth cut easier. On the contrary, the method generated wider kerf widths on the top surface, and a bigger HAZ was observed due to heat propagation on a wider area and the creation of melted residues.

The cutting process is primarily a two-phase process. Initiating the penetrating phase, the laser beam is used to form a keyhole still trapped inside the cutting zone. The shape of the keyhole as a still trap is similar to the blind hole, which has a high aspect ratio, as shown in Fig. 7. However, as the cutting speed increases, the cutting pressure inside the region increases, and the trap hole may become unstable. The instability arises owing to uneven and random interactions of reflected and incident beams inside the hole, which have uneven sidewalls, thus leading to excessive heat accumulation in the region in random directions. This also deteriorates the sidewalls of the cutting section. High-intensity and continual application of the laser passes leads to further deterioration of the surfaces. During each laser pass time interval, the vapour pressure has a reverse influence on the cutting surface quality.

This is followed by the second phase, which starts when full penetration is accomplished. At low cutting speed (E1: 5 mm/min), the laser beam penetrates completely, and the molten material is ejected by the created pressure, resulting in an improvement in the cutting quality. On the contrary, by increasing the traverse speed (E2: 10 mm/min, E3: 20 mm/min), owing to lower interaction time, the interaction over the main stream and the cut surface is not sufficient in terms of required heat transfer, thus the first phase remains incomplete (incomplete penetration). Thus, subsequent increases in the number of laser passes and additional recoil pressure may only deteriorate the cutting quality.

In contrast, HAZ was highly dependent on the number of passes, whereby  $N=6$  (E3) shows a much larger HAZ

compared to  $N=1$  (E1) due to the higher thermal conductivity of Si. This enhances the temperature gradient in the substrate with dependency on the material thermal conductivity ( $K$ ), specific heat ( $C$ ), density ( $\rho$ ), and time ( $T$ ), which defines the thermal penetration depth ( $\delta$ ) [45]:

$$\delta = \sqrt{\frac{K}{\rho C} T} \quad (1)$$

It is observed that higher thermal conductivity at higher processing times leads to more penetration of laser heat into the material.

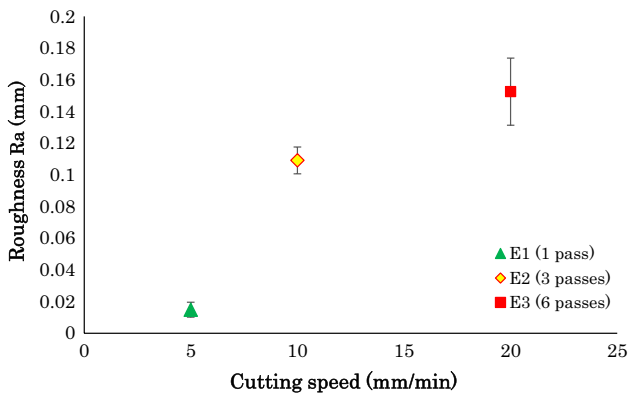
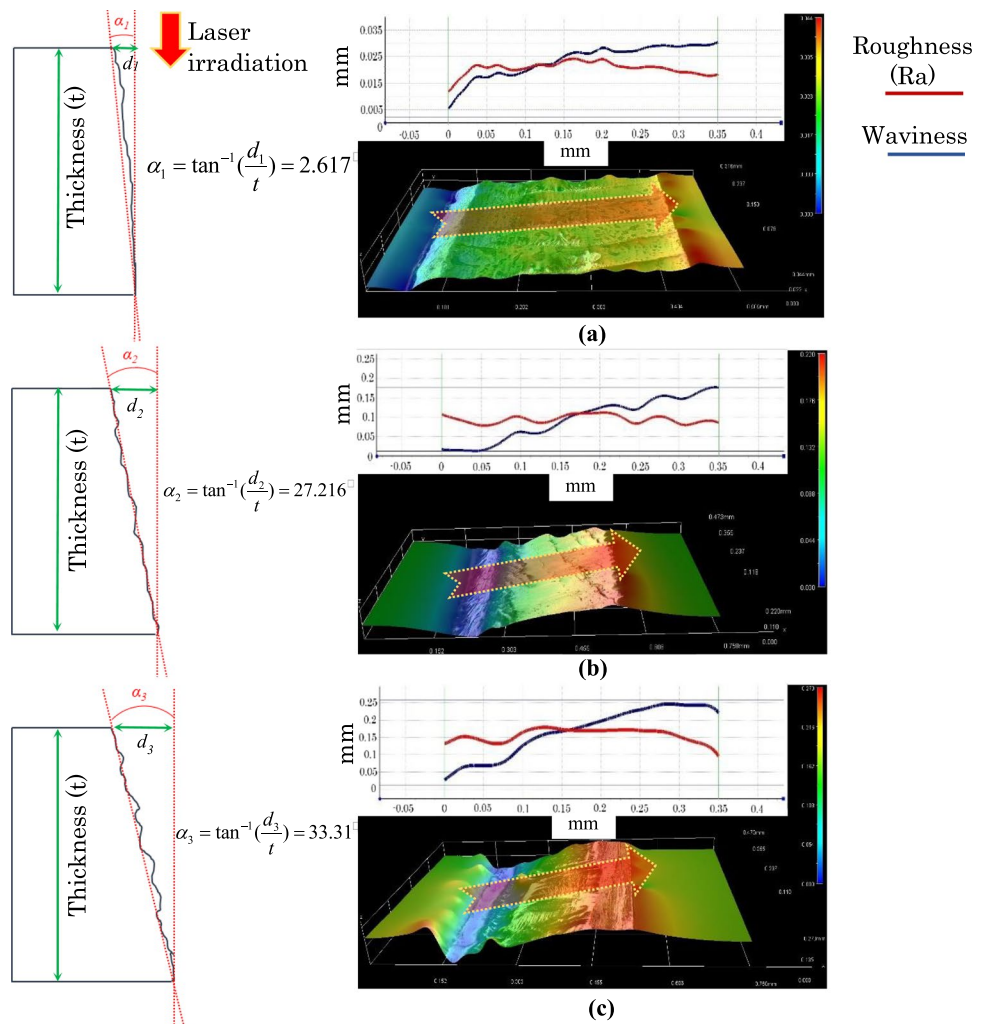
### 3.3 Surface roughness

Figure 8 represents the cross-sectional 3D surface topography of each cutting strategy used for experimentation. The 3D digital microscope (HIROX RH-2000) was employed to capture this topography as well as quantify surface roughness and waviness. Surface roughness and waviness were plotted through the transparent red arrow shown on the cross-section topography. With the advancing laser beam spot, the melt pool starts solidifying immediately as the residues in contact with the melted zone show the re-solidification owing to their partial melting. The irregular portion of the residuals at the edges of the melt pool leads to higher surface roughness behaviour. The surface quality is highly improved at low speeds of cutting (5 mm/min) at a single pass (Fig. 8a). With an increase in either cutting speeds or the number of passes, the surface quality degrades significantly. Figure 8b shows that with a twofold increase in cutting speed and triple the number of laser scans, the surface roughness in specimen E2 increased. Accordingly, for specimen E3, Fig. 8c indicates a significant increase in surface roughness by increasing the cutting speed to 20 mm/min and the number of passes to 6, which ascertains a lesser quality surface due to heat accumulation and the creation of more solidified residues.

The mean value of surface roughness for each experiment was also measured, as shown in Fig. 9. The average roughness is lowest for E1, followed by the average/median value for E2, and highest for E3. Thus, results support the claim that the better quality of sidewalls was obtained by decreasing the cutting speed at a single laser scan. It provided enough time for the laser beam to get through the Si thickness, melt the stimulated material elements, and create the whole cut by expelling the melted substance. However, at high cutting speed, the quality of the sidewall was diminished significantly with the increase in multi-passes.

The morphology of the actual surface generated on the samples was obtained from the sample shown in Fig. 2d, h, l. The partial melt zone and associated solidified particles cause poor finish in the laser cutting, as evident. As Si has

**Fig. 8** The typical surface topography cross-section measurement of laser cutting of silicon wafer (taken from cross-sections shown in Fig. 2d, h, l, respectively), including sample waviness and roughness graph based on specified directional arrow using optical microscope. **a** E1 ( $V=5$  mm/min;  $N=1$ ). **b** E2 ( $V=10$  mm/min;  $N=3$ ). **c** E3 ( $V=20$  mm/min;  $N=6$ )



**Fig. 9** Average surface roughness for different laser cutting speeds and number of laser passes

a higher melting point, the partial melting phenomenon is more common in such a scenario. Moreover, the deposition rates in experiment E3 (Fig. 8c) are higher compared to E1 and E2 (Fig. 8a, b, respectively), causing higher regular

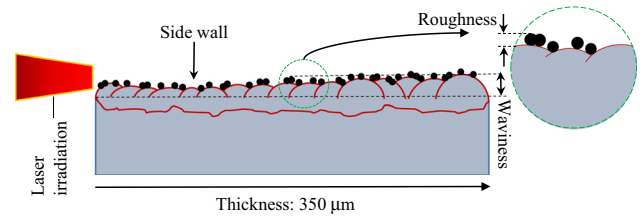


**Fig. 10** Schematic view of surface roughness and waviness

interval fluctuations due to serious deposited residues and black spots induced by a laser beam. The observed regular interval fluctuations, also sometimes referred to as waviness and previously shown by Micallef et al. [46], are not included in the calculation of roughness estimates while having measurements for the surface roughness. However, the impact of such waviness is detrimental to the life of the prepared component and its real-time applications. A schematic diagram for roughness and waviness is shown in Fig. 10.

An important finding from waviness graphs is to discover the possibility of a straight cut for each experiment, which is crucial for the micromachining of high-tech industries. The perpendicularity can be measured based on the deviation from the top surface, taken as the reference point for longitude, to the bottom surface. This is also known as the kerf taper angle, as discussed by previous researchers [47, 48]. It acts as a quality identifier for laser cutting. Liu et al. [47] showed that cutting speed has a significant impact on kerf taper. Reduced cutting speed increases the input energy, therefore stimulating the complete vaporisation of the target material from the bottom kerf. Consequently, the kerf taper decreases significantly. In another study performed by Mustafa [48], higher cutting speed caused an increase in the taper angle owing to a reduction in the interaction time between the laser beam and the cutting zone. The current study shows that once lower cutting speeds and single passes (E1) are employed, the taper angle of the cutting section is mostly near  $0^\circ$  (Fig. 8a;  $\alpha_1 = 2.617^\circ$ ), which indicates that the edge of cutting surface is perpendicular to the top surface. Whereas, in samples E2 and E3, by applying higher value of cutting speed and with more passes, the taper angle deviates significantly from  $0^\circ$ , and an inclined plane is created (Figs. 8b, c;  $\alpha_2 = 27.216^\circ$  and  $\alpha_3 = 33.31^\circ$ , respectively). This can be explained with the gradual defocusing of the beam, which is initially focused at the top surface of a 350- $\mu\text{m}$ -thick silicon plate. With the formation of depth of cut, the laser beam is gradually defocused, especially for full depth of cut. At the beginning, the incident beam is at an angle of around  $0^\circ$  with reference to the top surface of the substrate. During this period, most of the incident energy of the laser beam was absorbed by the material, irrespective of speed, number of passes, etc. Upon ablation, the top surface is gradually removed, and a hole/groove is formed. This leads to the interaction of the laser beam with sub-surface regions, generating deeper cavities, especially when lower cutting speeds are used. Thus, the incident angle swiftly shifts from zero to near  $90^\circ$ . In addition, since the starting focus was the top surface, it is inevitable that the taper angle will be generated, which cannot be avoided in such a scenario.

### 3.4 EDX analysis

The EDX analysis was also performed to study the elements on the surface of the specimen after laser cutting, as shown in Fig. 11. The SEM image was taken from the top-cut surface of sample E1, corresponding to sound laser cutting. A certain area on the laser cutting surface was selected, and compositions were measured using the EDX, as shown in Fig. 11a. The analysis revealed that the cutting surface mainly contains Si and C (Fig. 11b). The reason can be found in decomposing into  $\text{SiO}_2$  and carbon oxides due to

burning and highly induced heat by laser. It was shown by Osipov et al. [49] and Ma et al. [50] that when Si wafers are exposed to laser irradiation below the damage threshold, a thin surface layer undergoes a chemical transformation, and Si may react with the ambient air to form compounds like silicon dioxide (silica). In this case, due to the presence of some defects induced by laser, the original crystal shape of the Si wafer alters and the bonds of two adjacent Si atoms become broken, resulting in dangling bond formation. Due to the presence of oxygen ions surrounding the regions of silicon material under laser irradiation, the dangling bond has the capacity to trap the oxygen atoms, and therefore, the oxygen is incorporated into the Si wafer surface. On the other hand, the laser cutting process creates a localised high-temperature zone, specifically near the cutting region. In such a high-temperature environment, carbon can diffuse and migrate into the Si wafer structure. It results in the formation of silicon carbide (SiC) when carbon reacts with Si under high-temperature conditions. It is also noted that, despite the fact that the surface of the Si wafer was cleaned strictly before the laser processing, the presence of residues, oils, or particles during handling of the substrate may cause the release of carbon atoms when the high-intensity laser beam combusts these contaminants. The chemical compositions, calculated in the weight percentage, are given in Table 2. The findings of Uddin et al. [51] show similar chemical compositions, while they have used traditional cutting of silicon wafer. Although the  $\text{CO}_2$  laser is a non-contact heat source and it increases the material temperature to make a removal process, it is found that the increased interface temperature for both methods results in chemical affinity at high temperatures. In addition, the sample was mapped and line-scanned to observe particles distribution of other materials in the region induced by laser heat and its adjacent area. The distributions of silicon (Si) and carbon (C) particles are represented in blue and red colours in Fig. 11d, respectively. Oxygen (O) is shown in green. It is observed that major elements are Si particles, which is also confirmed by line-scan analysis (Fig. 11c).

## 4 Numerical analysis

In this section, a simplified model of the experimental process is discussed to demonstrate the distribution of temperature gradients and to provide stress variations that can result in a proper understanding of the cutting characteristics of the experimental process. The results encompass various key parameters such as temperature profiles, surface quality metrics, stress gradients, and element removal. The three-dimensional mathematical model of workpiece material during laser cutting is described, and the numerical method based on the finite element method (FEM) is outlined. ABAQUS,

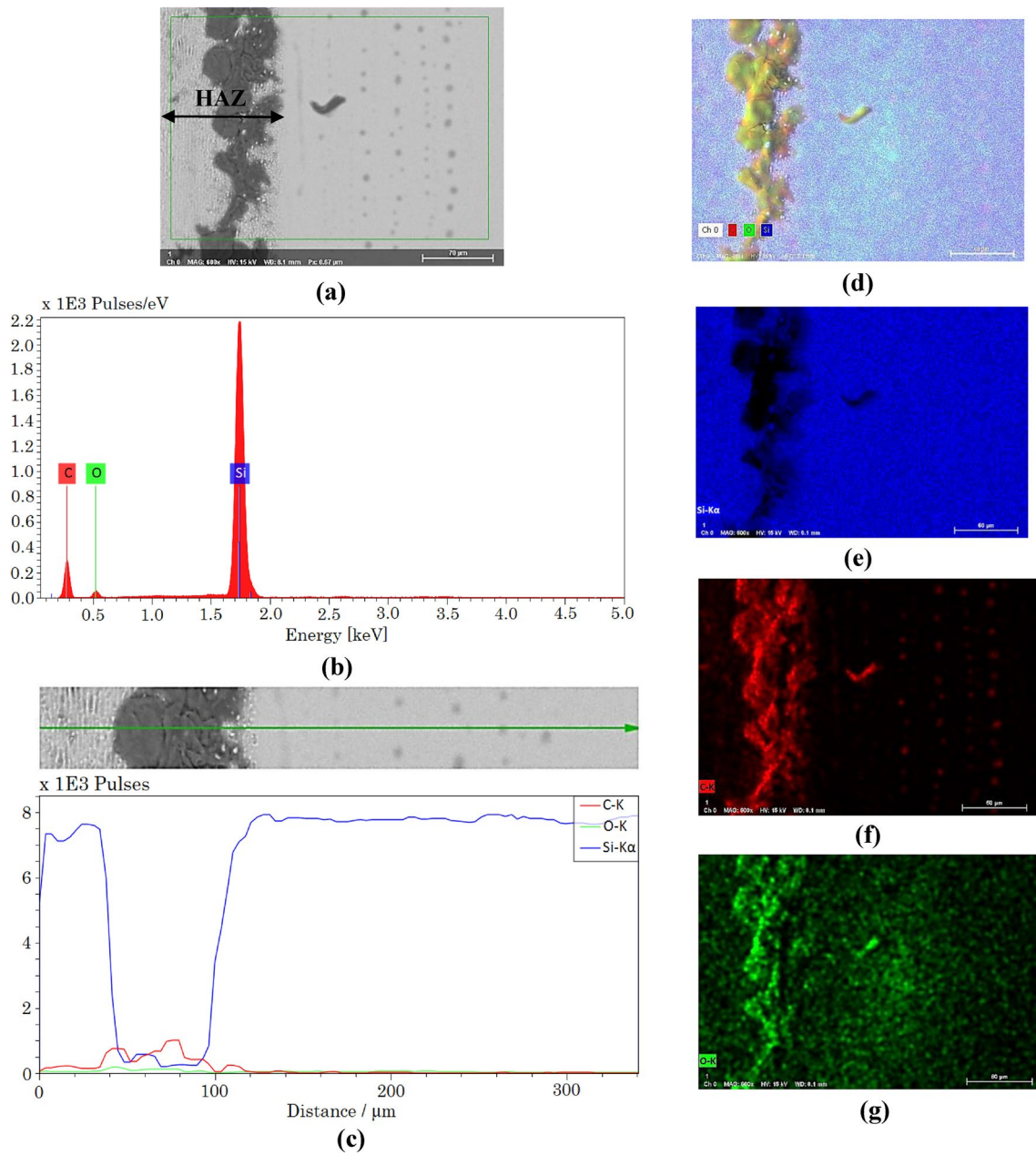


**Fig. 11** **a** Selected SEM micrograph and element distribution for EDX measurement of experiment E1. **b** Spectrum E1. **c** Line scan of specimen E1. **d** Overall mapping of specimen E1. **e** Si individual of specimen E1. **f** C individual of specimen E1. **g** O individual of specimen E1

**Table 2** EDX result in weight%

Area	Silicon (Si)	Carbon (C)	Oxygen (O)
Spectrum E1	66.3%	30.6%	3.1%

a commercially available FE analysis tool, is employed to calculate the thermally generated stress distribution and subsequent element removal process for Si wafers. The proposed model differs from previous simulation work in laser

cutting of Si wafers considering LITP [12–14], which primarily centred on utilising the XFEM method and assessing the stress intensity factor. Here, the main focus is on utilising the threshold value for the elemental failure criterion of Si under combined stresses generated by thermal/mechanical loads with the estimation of the spatial and temporal removal of elements upon failure. This makes the numerical simulation more realistic as the actual process of material ablation and removal is practically similar in nature (as discussed in Sect. 4.3). Before simulating the temperature and stress

distribution, a list of basic assumptions and considerations are summarised below:

- 1 The workpiece is assumed to be homogeneous, isotropic material with no defects.
- 2 The effects of gravity, support-driven forces, friction between the supports and workpiece, and other such causes of residual stresses are ignored. Moreover, the strain caused by creep is also not considered owing to shorter thermal cycles at the peak temperature.
- 3 Parameters that are set constant in the simulation model include laser power, laser cutting speed, laser beam spot diameter, ideal Gaussian distribution, and convectional heat transfer coefficient. The absorptivity coefficient is considered temperature-dependent. Moreover, beam quality is ignored here.
- 4 Material properties are defined, including density, which is set as constant; specific heat; thermal conductivity; Young's modulus and Poisson's ratio of Si; thermal expansion coefficient; Johnson–Cook (J-C) plasticity; and fracture model for element failures (to remove the elements that have lost their strengths via ablations). All other parameters are ignored or set as zero.
- 5 Since fluid flow is not simulated, the melt pool and associated physics of pressure distribution leading to vaporisation are not considered here.

Using the previously published works and guide, the laser radiation introduced a thermal-induced tension on the area under consideration. This tension begins as a progressive crack process leading in the direction of the laser on the wafer surface. However, due to the limitations of the defined material model, the material removal and the actual laser cutting process were not elucidated properly. However, the process is highly coupled, involving laser material processing, heat transfer along the moving source, followed by material ablation and removal. Here, a commonly used approach of sequentially coupled thermal and mechanical analysis is used, which was previously successfully done by Cai et al. [11], Moghadasi et al. [52], and Moghadasi et al. [53]. Thus, initially, a 3D transient thermal analysis is carried out, and the thermal map is then used for mechanical load and stress evaluations. The flowchart of the simulation process is shown in Fig. 12. It is seen that after the model preparation, a sequential coupling of the thermal-stress method is adopted, which consists of two phases: (i) heat transfer calculation and (ii) thermal-stress and mechanical failure calculation. The first phase is heat transfer analysis. The DFLUX user subroutine is used to calculate the temperature field based on the Fourier heat transfer model. Upon heat transfer calculation, stress and damage-failure propagation analysis are carried out in second phase. Temperature-driven thermal stress is applied to the system to perform

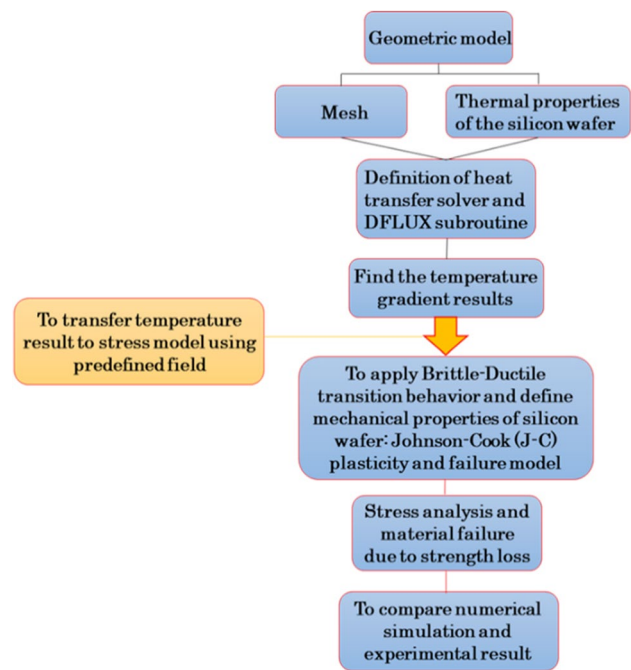


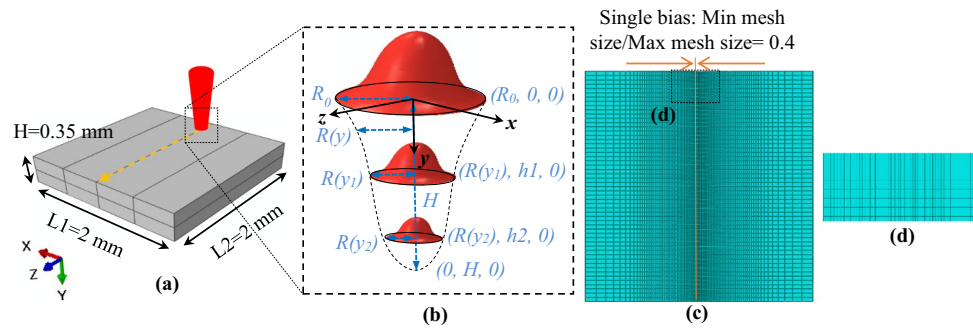
Fig. 12 The flow chart of the simulation procedure

mechanical failure calculation and its dynamic damage propagation, which help finding stress variations and HAZ. The stress field and damage propagation pattern are calculated using the J-C failure model approach. This phase uses the elastoplastic model and temperature-dependent parameters.

#### 4.1 Mesh and model

For the present study, hexahedron-type mesh cells are employed using the Hex-dominated method. The element selected for the heat transfer analysis is an eight-node linear convection/diffusion element (DCC3D8). In order to demonstrate the transient non-linear stress analysis of laser cutting process behaviour, an explicit physics option is preferred for all simulated cases. The use of an eight-node brick element (C3D8R) allows hourglass control along with reduced integration, which is useful for stress analysis. At places deemed to have higher gradients and transitional behaviour, relatively finer meshes are employed compared to other locations. The model dimension and mesh properties are shown in Fig. 13. In this study, the sample is modelled in a rectangular shape with dimensions of  $2 \times 2 \times 0.35 \text{ mm}^3$ . Figure 13a shows the created model in ABAQUS. A denser number of elements is found adjacent to the cutting region to achieve accurate results (Fig. 13c). The total number of nodes is 90,695, while there are a total of 82,944 elements. Figure 13d shows the magnified zone of cutting involving denser mesh with a bias number of 0.4. With a quad-core processing unit having 32 GB of RAM (high computing

**Fig. 13** **a** The square shape of the mathematical model for silicon wafer. **b** Laser beam shape and its intensity through the thickness. **c** Mesh distribution. **d** Mesh density along the cutting line



facility), the single analysis took an estimated 20 clock hours.

## 4.2 Thermal mechanisms

### 4.2.1 Heat transfer equations

The mathematical model for transient heat transfer needed for laser material processing involves (i) heat conduction within the workpiece and (ii) heat transfer to the surroundings through convection and radiation modes, as illustrated in Fig. 1c. The three-dimensional variations of the time-dependent temperature profile  $T(x, y, z, t)$  in the specimen are given by Eq. (2) along with the initial as well as boundary conditions:

$$\frac{\partial}{\partial x} \left( K \frac{\partial T}{\partial x} \right) + \frac{\partial}{\partial y} \left( K \frac{\partial T}{\partial y} \right) + \frac{\partial}{\partial z} \left( K \frac{\partial T}{\partial z} \right) + Q + Q' = \rho C_p \frac{\partial T}{\partial t} \quad (2)$$

where  $\rho$  is the density of the material ( $\text{kg/m}^3$ ),  $K$  is the thermal conductivity ( $\text{W/m K}$ ),  $C_p$  is the specific heat capacity ( $\text{J/kg K}$ ),  $T$  is the temperature ( $\text{K}$ ),  $t$  is the time variable ( $\text{s}$ ),  $Q$  is the amount of heat generated per unit volume due to laser irradiation,  $Q'$  is the internal heat source, which is null (owing to the absence of internal heat generation by Si), and  $k \frac{\partial T}{\partial y}$  (known as  $Q_v$ ) is the heat loss due to heat convection. Considering the Si surface as the main heat loss area while other surfaces are insulated (i.e. adiabatic), the corresponding boundary condition by considering  $Q_v$  as the heat loss is given by:

$$-k \frac{\partial T}{\partial y} \Big|_{\Sigma} = h_{\text{conv}}(T_s - T_{\text{env}}) + \epsilon \sigma (T_s^4 - T_0^4) \quad (3)$$

where  $h$  is the heat transfer coefficient due to natural convection,  $\epsilon$  is the emissivity,  $\sigma$  is the Stefan–Boltzmann constant,  $\Sigma$  is the external boundaries of the substrate, including the top surface, the bottom surface, and the surrounding surfaces of the silicon layer, and  $T_s$  and  $T_0$  are respectively the surface and the initial temperatures ( $\text{K}$ ).

### 4.2.2 Heat source equations

The accurate prediction of the thermal field and subsequent damage/loss of material highly relies on the heat profile. Here, the following heat flux model is used, concentrating at the centre and varying exponentially as  $R$  increases:

$$Q = \frac{aP}{\pi R_0^2} \times \exp \left[ -B \left( \frac{R}{R_0} \right)^2 \right] \quad (4)$$

$Q$  represents laser intensity, while the material property of absorptivity is given by  $a$ , and  $P$  represents the laser power. The beam spot has  $R_0$  as the radius, with  $R$  being the distance to the beam centre. The shape factor of the Gaussian heat flux is controlled using  $B$ , which is the shape factor. A schematic illustrates the three-dimensional heat flux as shown in Fig. 13b, which is modelled using the DFLUX routine to ensure conical shape of volumetric heat flux. The expression of the surface heat flux density is:

$$Q = \frac{aP}{\pi R^2 H} \times \left( 1 - \frac{y}{H} \right) \exp \left[ - \left( \frac{(z - z_t)^2 + (x - x_t)^2}{R_0^2} \right) \right] \quad (5)$$

where  $H$  is the sample thickness, and  $z_t$  and  $x_t$  are the locations of the laser along the cutting line at a specified cutting speed ( $v$ ). As previously discussed in Sect. 1, crystalline Si absorbs very little radiation at the  $10.6\text{-}\mu\text{m}$  wavelength and room temperature, unless free carrier absorption is enhanced by temperature or through doping level [26, 54]. Therefore, for absorptivity  $a$ , the finding discussed by Boyd et al. [27] is considered to define temperature-dependent absorption coefficient (For the sake of brevity, the readers are encouraged to see the Supplementary information (SI) for additional discussion). The properties of the material are given in Table 3 [55–58].

**Table 3** Thermal and mechanical properties of Si wafer

$T$ (°C)	Density (kg/m <sup>3</sup> )	Specific heat (J/kg °C)	Thermal conductivity (W/m °C)	Young's modulus (GPa)	Poisson's ratio	Expansion coeff. alpha (10 <sup>-6</sup> /°C)
25	2329	713	148.0	165.6	0.28	2.63
125	–	788	98.9	164.3	–	3.23
225	–	830	76.2	162.9	–	3.60
325	–	859	61.9	161.5	–	3.83
425	–	887	51.0	160.1	–	4.01
525	–	908	42.2	158.7	–	4.14

### 4.3 Stress (mechanical) mechanism

In laser processing, with the melting of material, the heat is absorbed during phase change. This leads to stress formation owing to the thermal gradient and leads to residual stress appearance in subsequent laser passes. Therefore, the temporal-spatial variations of temperature from each step of thermal analysis are used as input for stress analysis, while the same mesh characteristics were employed to avoid interpolation and mapping challenges.

#### 4.3.1 Mechanical behaviour formulation

For stress analysis, the quasi-equilibrium approach is used:

$$\nabla \cdot \sigma + f = 0 \quad (6)$$

where  $\sigma$  is denoted as the Cauchy stress tensor and  $f$  is the body force tensor. The mechanical constitutive law can be defined as:

$$\sigma = [D]\{\varepsilon_{el}\} \quad (7)$$

where  $D$  is denoted as the fourth-order elastic tensor and  $\varepsilon_{el}$  is the elastic strain tensor calculated by:

$$\varepsilon_{el} = \varepsilon_T - \varepsilon_P - \varepsilon_{thermal} \quad (8)$$

where  $\varepsilon_T$ ,  $\varepsilon_P$ , and  $\varepsilon_{thermal}$  are denoted as total, plastic, and thermal strain tensors, respectively. The thermal strain tensor is defined as:

$$\varepsilon_{thermal} = \alpha(T)(T - T_R)\mathbf{I} \quad (9)$$

where  $\alpha$  is the temperature-dependent thermal expansion coefficient (1/K),  $T$  is the local element temperature (K),  $T_R$  is room temperature, and  $\mathbf{I}$  is the identity tensor (The equations for large deformations are seen in the SI as additional discussion).

#### 4.3.2 Brittle-to-ductile transition

At room temperature, single crystal Si exhibits brittleness, and its crack propagates without significant plastic deformation due to the presence of sp<sup>3</sup> bonding and the crystalline cubic diamond structure of Si. It is widely recognised that specific materials undergo significant changes in mechanical behaviour in response to variations in factors such as temperature, strain rate, and others. One of the most noteworthy expressions of such mechanical variability is the transition between brittle and ductile behaviour (BDT), commonly observed in various engineering materials. The pivotal determinant influencing the brittle or ductile characteristics of materials is the nature of the atomic bonds. Bond types with greater electron mobility tend to promote ductile behaviour. Conversely, restricted electron mobility contributes to brittle characteristics. Given that metallic bonds (ionic bonds) exhibit higher electron mobility, they are conducive to the material's ductile response, whereas covalent bonds, characterised by limited electron movement, result in brittle behaviour. In this context, Si demonstrates robust directional covalent bonds within the structure of a diamond. Consequently, at room temperature, dislocations remain immobile, rendering silicon's response brittle. However, it displays metallic ductile behaviour above a certain temperature. Dislocations of Si can only be activated at a high temperature (> 600°C), based on findings discovered by Yan et al. [59]. By transitioning to the ductile mode, Si is deformed plastically and removed when stresses meet the failure requirement, while in a brittle state, material removal occurs by creating cracks on both the surface and subsurface. To achieve high-precision engineering in Si wafer machining, it is preferred to explore the ductile mode. This is why the transition from BDT material removal mode has been extensively studied through both experimental investigation and numerical simulation.

### 4.3.3 Plasticity behaviour and failure criteria

The establishment of an appropriate Si constitutive model is a critical step to achieving accurate stress results. As for the thermo-mechanical problems, with the rising temperature, the bonds connecting material points keep expanding, which causes an increase of dislocation density in the microstructure, and the bonds are resultantly broken. This is the stage where the material transitions into the ductile phase, plastic behaviour starts, and eventually, by meeting the failure criteria, damage occurs [59, 60]. Therefore, the “Material Model: J-C Plasticity Model” module in the ABAQUS software was employed in this study. The general plasticity model of J-C is written as:

$$\sigma = [A + B\epsilon^N] \cdot \left[ 1 + C \ln \left( \frac{\dot{\epsilon}}{\dot{\epsilon}_0} \right) \right] \cdot \left[ 1 - \frac{T - T_R}{T_M - T_R} \right] \quad (10)$$

where  $A$ ,  $B$ , and  $C$  are material parameters measured at room temperature.  $T$ ,  $T_R$ , and  $T_M$  denote the operating temperature, room temperature, and melting temperature, respectively. Subsequent to the plasticity model, a failure growth criterion is established in this study based on accumulated damage as proposed in the J-C damage model [61]. The expanded form of Johnson and Cook’s (1985) basic model included the constitutive model for fractures and relating them to cumulative damage. Moreover, the expanded model included the multiplicative effects of stress triaxiality, strain rate, and local heating. For the J-C damage model, damage  $D$  is determined as:

$$D = \sum \frac{\Delta\epsilon_{pl}}{\epsilon_F} \quad (11)$$

where  $\Delta\epsilon_{pl}$  is the incremental effective plastic strain and  $\epsilon_F$  is the fracture strain. The general cumulative-damage fracture model for the fracture strain ( $\epsilon_F$ ) is given as:

$$\epsilon_F = [D_1 + D_2 \exp(D_3 \sigma^*)] \left[ 1 + D_4 \ln \left( \frac{\dot{\epsilon}}{\dot{\epsilon}_0} \right) \right] \left[ 1 + D_5 \left( \frac{T - T_R}{T_M - T_R} \right) \right] \quad (12)$$

where  $D1$ – $D5$  are the material constants in the J-C fracture model,  $\sigma^*$  is the stress triaxiality ratio defined as  $\frac{\sigma_m}{\bar{\sigma}}$ , where  $\sigma_m$  and  $\bar{\sigma}$  represent the average of the three principal stresses and the von Mises equivalent stress, respectively.  $\dot{\epsilon}$  and  $\dot{\epsilon}_0$  represent the equivalent strain rate and reference strain rate,

respectively. The mean values of  $D1$ – $D5$ ,  $T_M$ , and  $\dot{\epsilon}_0$  for the Si wafer substrate are shown in Table 4.

### 4.4 Morphology and temperature analysis

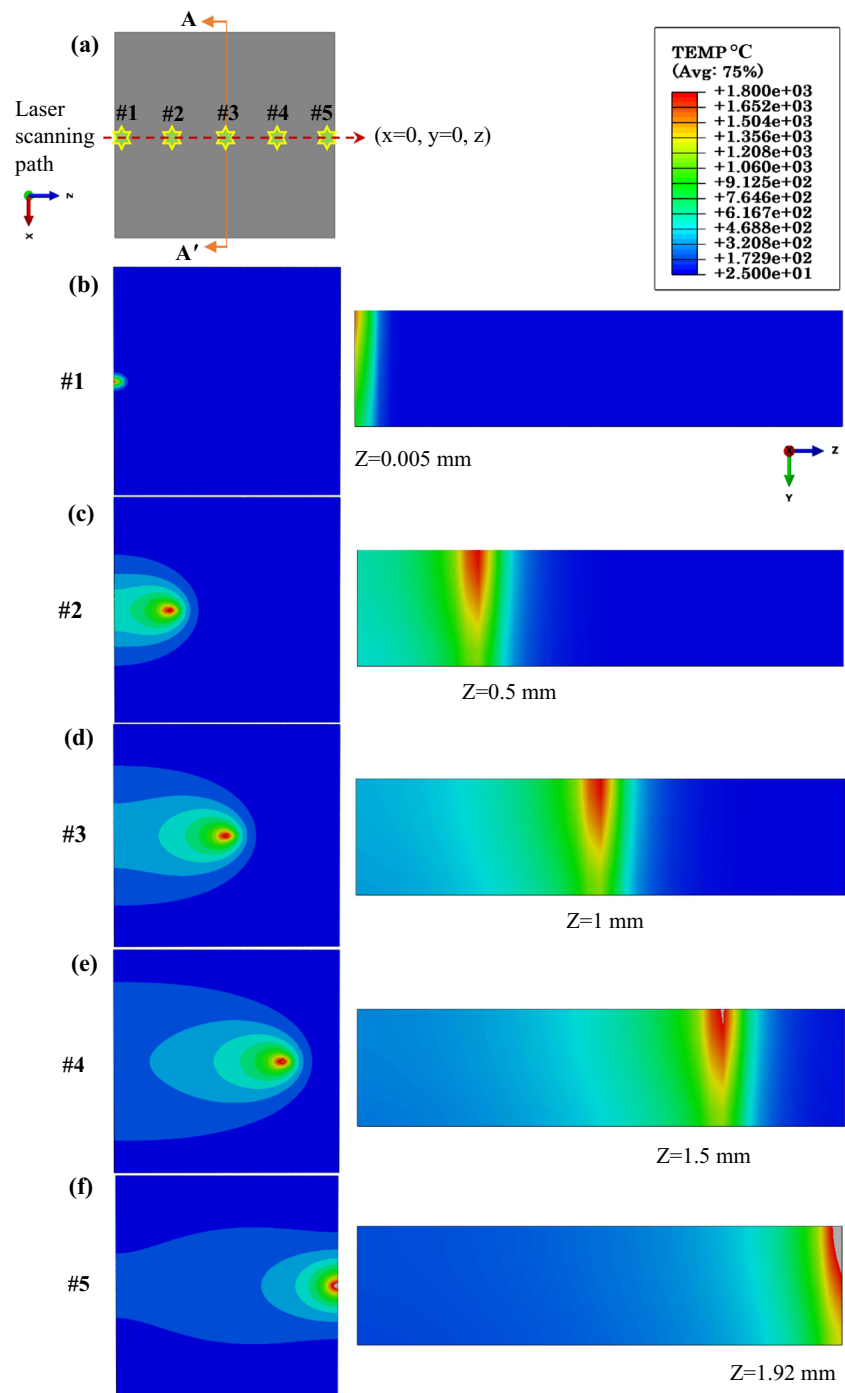
With the exposure of the isotropic workpiece to intense laser energy, the temperature gradient leads to the formation of the molten pool. As the transmitted heat flux gets transmitted to the inside of the material slab through diffusion, the material’s internal energy increases instantaneously. The simulations of the temperature gradient at five distinct  $z$  positions are shown in Fig. 14. The specified red line in Fig. 14a indicates the laser beam track of scanning. With the Gaussian distribution of energy, the central regions exhibit higher intensity. Accordingly, the elements located in this region approach the melting temperature to cause total material strength loss and lead to elements’ failure. With the tracing of the moving heat source, the elements of the specimen are heated accordingly, and the cutting line is created by removing elements whose strength loss has occurred. The value of the highest temperature along the direction of the heat source also increases as heat accumulates. This finding was indicated by other researchers using different types of materials, e.g. fibre-reinforced composites [62] and thermoplastics [63]. As shown in Fig. 14b, the temperature field with plot contours of reference case 1 rises quickly, when the laser is at position  $z = 0.005$  mm (at time  $t = 0.06$  s). Tracing the laser towards the scanning line for subsequent reference cases 2–5 shows that the rate of temperature change becomes relatively stable. It exceeds the melting point at  $1450^\circ\text{C}$ , as shown in Fig. 14b–f. The maximum recorded temperature is  $1585^\circ\text{C}$ , which is 9.3% higher than the melting point. However, despite disparities in the selected processing parameters and modelling methodologies between the present investigation and the studies conducted by Cheng et al. [14] and Cai et al. [11], a consistent pattern of temperature gradient emerges across all outcomes. Additionally, the correlation between the laser position and energy absorption indicates consistent peaks and valleys in the time history curves, as shown in Fig. 15a.

The rapid heating during laser processing is the result of the induction of a significantly high-temperature gradient. This gradient is usually ahead of the beam spot, and when the spot passes over the location, it rises and then exponentially lowers subsequently (Fig. 15a). Ahead of the laser source, the heat cannot be rapidly conducted or transferred; instead, the elements behind the source of laser beam lead to rather homogenised temperature field. Consequently, the melt pool shapes

**Table 4** Values of Johnson–Cook (J-C) plasticity and fracture model coefficients for the Si wafer material

Material	Coefficients of J-C plasticity model				Coefficients of J-C fracture model						
	$A$	$B$	$N$	$C$	$D1$	$D2$	$D3$	$D4$	$D5$	$T_M$	$\dot{\epsilon}_0$
Silicon	280	380	0.35	0.06	0.026	0.266	–0.512	0.017	0.05	1450	0.007

**Fig. 14** The simulations of temperature gradient at five distinct  $z$  positions. **a** Schematic view of five reference cases at different positions. **b** Temperature gradient of reference case 1 at  $z=0.005$  mm. **c** Temperature gradient of reference case 2 at  $z=0.5$  mm. **d** Temperature gradient of reference case 3 at  $z=1$  mm. **e** Temperature gradient of reference case 4 at  $z=1.5$  mm. **f** Temperature gradient of reference case 5 at  $z=1.92$  mm

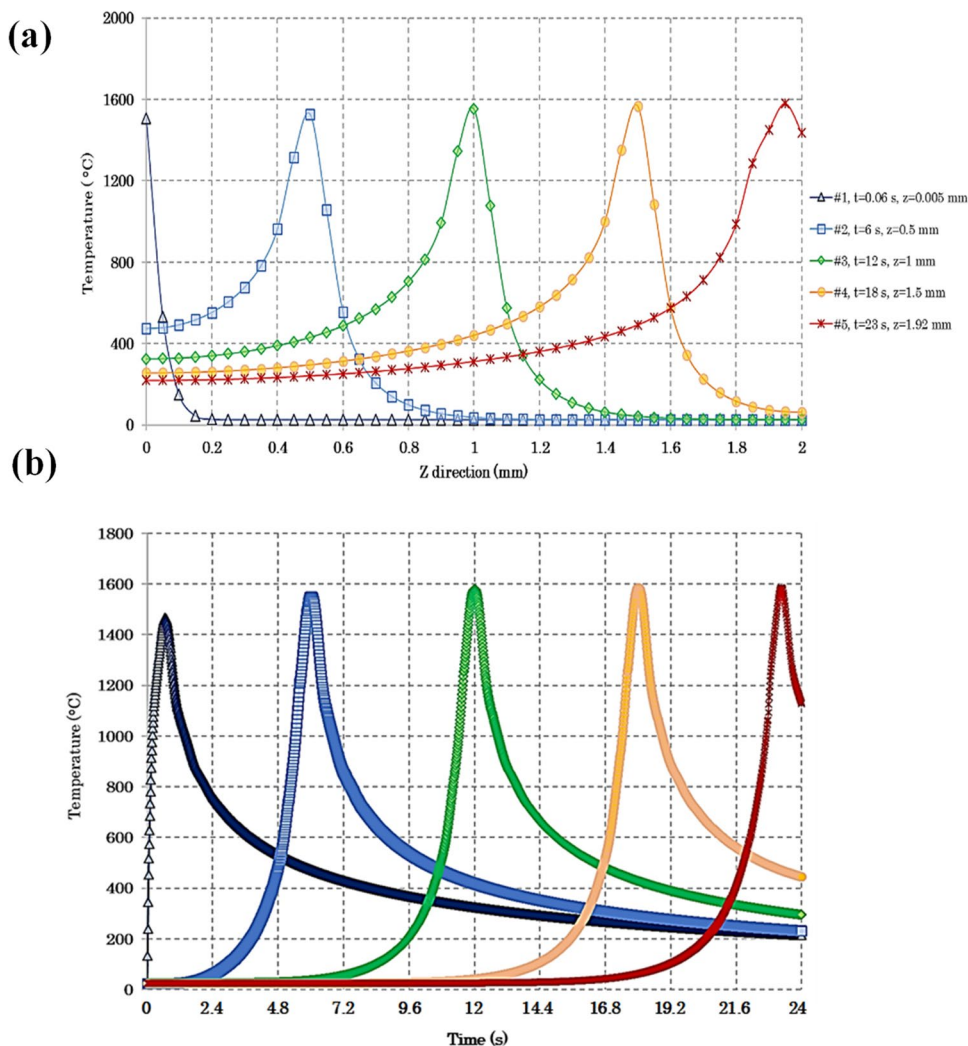


of cases 1–5 (Fig. 14b–f) show a long tail and a penetration through the thickness of the substrate. Dependant on the processing parameters such as laser power, reflection, interaction diameter, and material properties, the energy distribution is largely impacted by the scanning speed. Thus, using a controlled processing parameters tuning, the desired meltzone and pool can be relatively controlled.

On the contrary, the influence of cutting duration does not completely control the temperature distribution or

its peak value; rather, it depends on the thermo-physical properties of the substrate, which affects the temperature distribution. Figure 15b shows the thermal cycles in specified cases (1–5). The temperature profiles over time reach the maximum value when the laser meets specified cases. Moreover, after the operation of the laser passage, a gradual decrement in heating and cooling can be seen. For all regions in post-operation, the profile of temperatures

**Fig. 15** **a** Temperature profile for reference cases 1–5 on the laser scanning path. **b** Time history curves for reference cases 1–5



decreases at similar slopes and rates, as reported by Cai et al. [11] and Anjum and Shaikh [64].

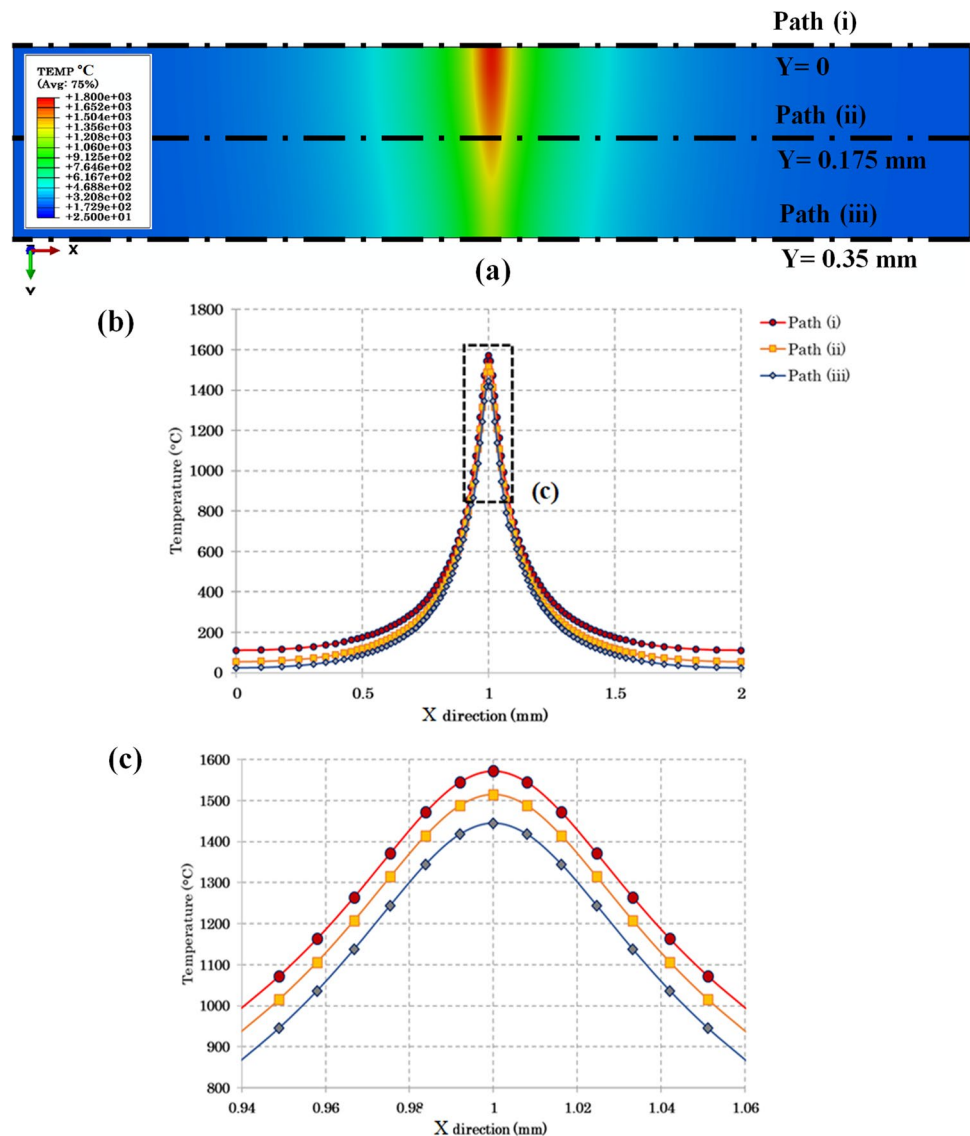
The transfer of heat along the thickness of the wafer exhibited through cross-section A–A' at  $t = 12$  s can be visualised using the temperature profile for the same predefined paths at the top (path i), middle (path ii), and bottom (path iii) of the cross-section surface, shown in Fig. 16a. The temperature profile for each path is presented in Fig. 16b. The temperature distribution is symmetric around the laser source, and the maximum temperature is found at peak laser fluence. In general, as the distance increases from the cutting line, the intensity of the heat gradient lessens and becomes flatter eventually. It is attributed to the influence of temperature on the specific heat capacity and thermal conductivity. These parameters impact the heat distribution in the material, in particular along the direction perpendicular to the laser scanning axis. The magnified Fig. 16c shows a closer look at temperature decay from top to bottom. It shows that the lowest

location passed melting temperature, resulting in element strength loss and its failure through the whole thickness.

#### 4.5 Stress analysis and material failure

During the laser cutting process, the Si wafer is subjected to thermal and mechanical stresses that can cause deformation, cracking, or even complete material failure. There are two types of stresses that occur during silicon wafer laser cutting: thermal stresses and mechanical stresses. Thermal stresses occur when the subsystem's electrons' temperature increases at a very high rate and causes expansion, which is due to the quick heating process corresponding to the laser. Mechanical stresses occur when the wafer is subjected to mechanical forces during the cutting process, such as from clamping. In order to assess stress levels, the prescribed displacement field and surface forces are used to calculate nodal displacements. The resulting strain and constitutive stress increments at all locations are then

**Fig. 16** **a** Temperature gradient through the thickness of the model. **b** Temperature graphs at different paths located on the top (path i), middle (path ii), and bottom (path iii) of the model. **c** Magnified picture of profiles at **(b)** for comparison of peak temperatures



evaluated through the process of interpolation. Local equilibrium conditions are maintained by correlating nodal displacements with enabling forces via the elemental stiffness matrix. Laser heating and resulting temperature fluctuations cause tensile and/or compressive stresses, which may adversely affect the quality of machined parts, particularly if thermal stresses exceed the critical values of the Si wafer. In such cases, permanent damage and/or fracture may occur. Therefore, it is crucial to closely monitor and control these stresses to prevent any negative impact on the finished product. To elucidate the impact of the scanning strategy on residual stress, an investigation is conducted on the transversal stress  $\sigma_x$ , the longitudinal stress  $\sigma_z$ , and the Mises stress  $\sigma_M$ . The stress components of  $\sigma_x$  and  $\sigma_z$  are represented for selected elements on the surface of cutting when the laser irradiates at specific locations. Mises stresses are presented through the thickness of the selected

paths shown in Fig. 16a having positive values for tensile and negative values for compressive stresses, respectively.

Figure 17a shows the transversal stress  $\sigma_x$  versus temperature gradient of a selected element at  $z=0.005$  mm in line with the cutting path. By entering the laser into the material, the elements are thermally shocked due to an immediate temperature increase. This phenomenon results in stress variations when the laser enters the specimen, as displayed in Fig. 17b. Primarily, tensile stresses are generated on the surface region of the irradiated object as the temperature rises, causing expansion of the elements. The maximum amplitude is 40.1 MPa. By propagating a stress wave into the material thickness and adjacent elements and increasing temperature, the specimen near the cutting region enters the compression phase. The peak magnitude of compressive stress is obtained at  $-130.3$  MPa, and it is followed by a significant drop to  $-70.8$  MPa. The graph

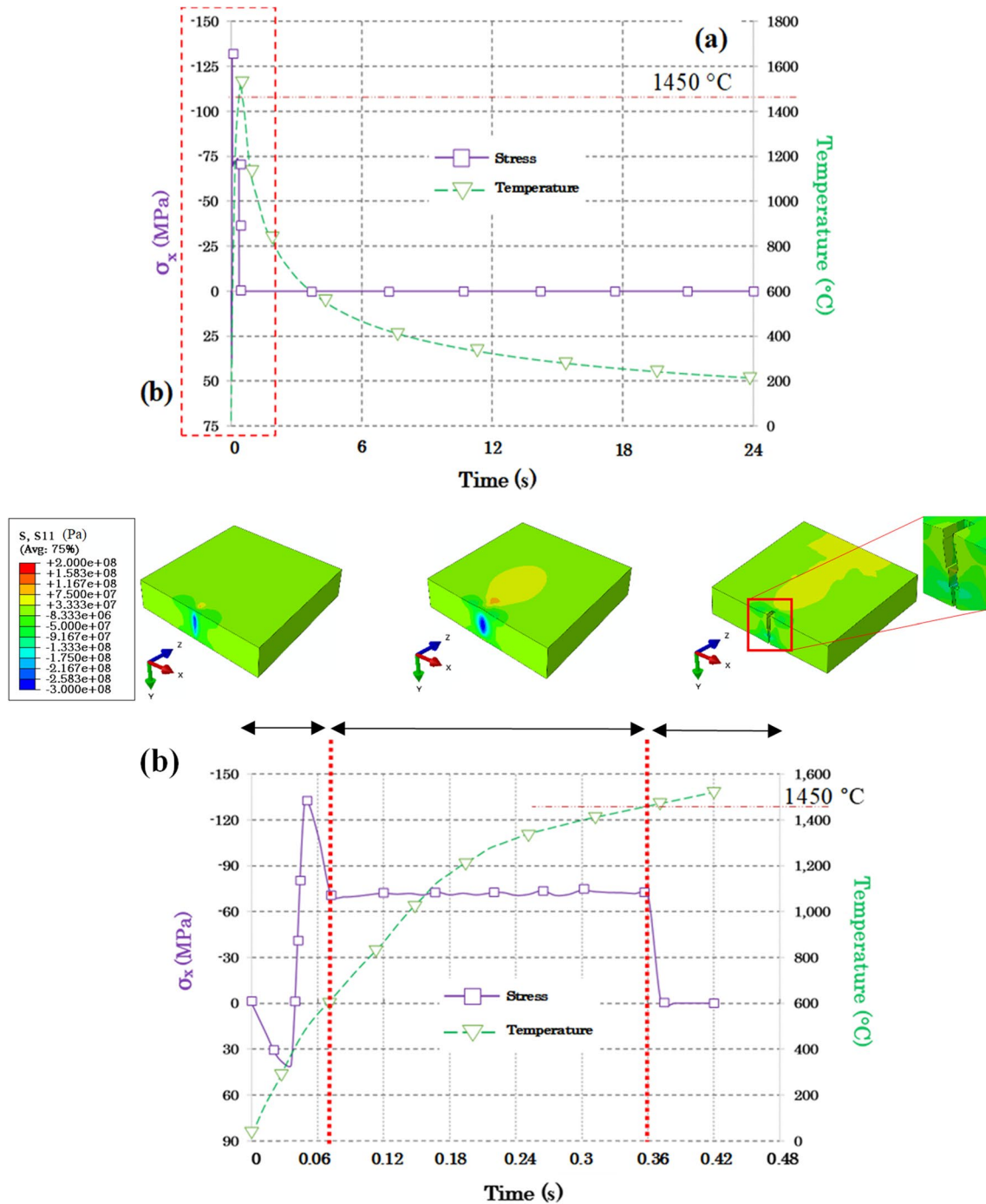


**Fig. 17** **a** Transverse stress ( $\sigma_x$ ) versus temperature history for an element on cutting line at  $z=0.005$  mm. **b** Magnified graph to see different steps of stress variation and element strength loss by increasing the temperature

indicates that for a short period of time, as the temperature increases from 600 to 1450  $^{\circ}\text{C}$ , the level of compressive stress continues to increase constantly until it decreases dramatically and becomes zero. It is inferred that the material strength loss is highly stimulated by passing the temperature from the melting point, which causes fracture initiation and resulting failure of elements parallel to the

laser scanning line. It entails element removal from the cutting line. The captured results from the simulation obviously show the process of element removal from the specimen at different stages. Similarly, it is seen as ejected or exfoliated of complete layers of material from the surface in the experiment's microstructure (Figs. 2 and 5).

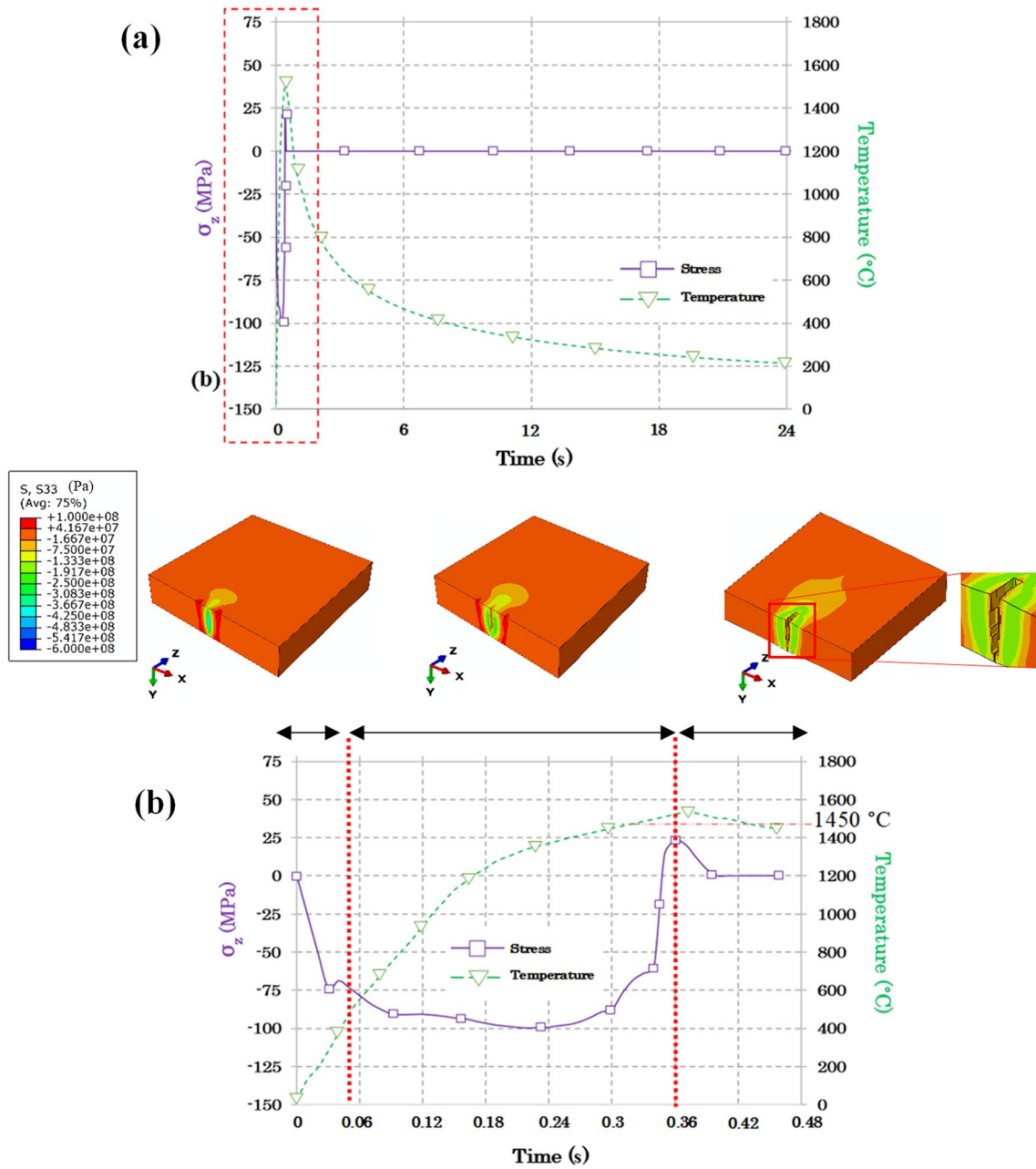


**Fig. 18** **a** Longitudinal stress ( $\sigma_z$ ) versus temperature history for an element on cutting line at  $z=0.005$  mm. **b** Magnified graph to see different steps of stress variation and element strength loss by increasing the temperature

Similarly, longitudinal stress  $\sigma_z$  versus temperature gradient is represented in Fig. 18a. However, the peak magnitudes of longitudinal stress  $\sigma_z$  are substantially lower than the transversal stress  $\sigma_x$ . At higher temperatures, the anisotropic thermal expansion of the material, especially along the dominant direction of heat transfer, results in lower longitudinal stress  $\sigma_z$  compared to transverse stress  $\sigma_x$ . As the laser beam heats up the material, the heat is predominantly transferred in the longitudinal direction. This results in material expansion in the same direction and, resultantly, stress

distributions that are anisotropic owing to thermal boundary conditions. Owing to the sharp gradient in the transverse direction (perpendicular to the laser beam) and restrained by the solid, unmelted material, the usual thermal expansion is restricted, resulting in higher stress levels in the transverse direction compared to the direction along the beam (longitudinal direction). In addition, the focused beam, in terms of the spot, causes an elliptical power density distribution. This may also result in a relatively imbalanced higher power density distribution, particularly in the transverse/

major direction than in the longitudinal/minor direction. The complete comparison was done by Abadi et al. [65]. Moreover, it is known that heated material with thermal expansion usually helps in alleviating stresses, whether tension or compression stress. Upon expansion, the strain energy is released under the influence of external factors. This may also alleviate some of the longitudinal stresses compared to transverse stresses, especially at very high operating temperatures. The effect of thermal expansion was previously discussed by Soltani et al. [41], whereby it was noted that the large temperature operations on the irradiated surface caused localised expansions and led to changes in density and subsequent thermal crack generation. It is shown in Fig. 18b that  $\sigma_z$  initially displays compressive behaviour,

and the maximum magnitude is achieved at  $-99.4$  MPa. Rising temperatures up to  $T \geq 600^\circ\text{C}$  increase the ductility of the Si wafer considerably and start decreasing the material's strength. Therefore, it is seen that when the temperature gets higher than  $600^\circ\text{C}$ , the plotted values for material compressive stress predominantly remain consistent. It can be inferred that when the material is increasingly heated, it undergoes a phase change from an elastic behaviour to a complete plastic state. During this phase change, the material's physical properties, such as strength and stiffness, degrade dramatically, and the rate of plastic strain increases. In particular, the material's ability to withstand compressive stress decreases significantly. Subsequently, by reaching the melting temperature ( $1450^\circ\text{C}$ ), the material's ability to resist

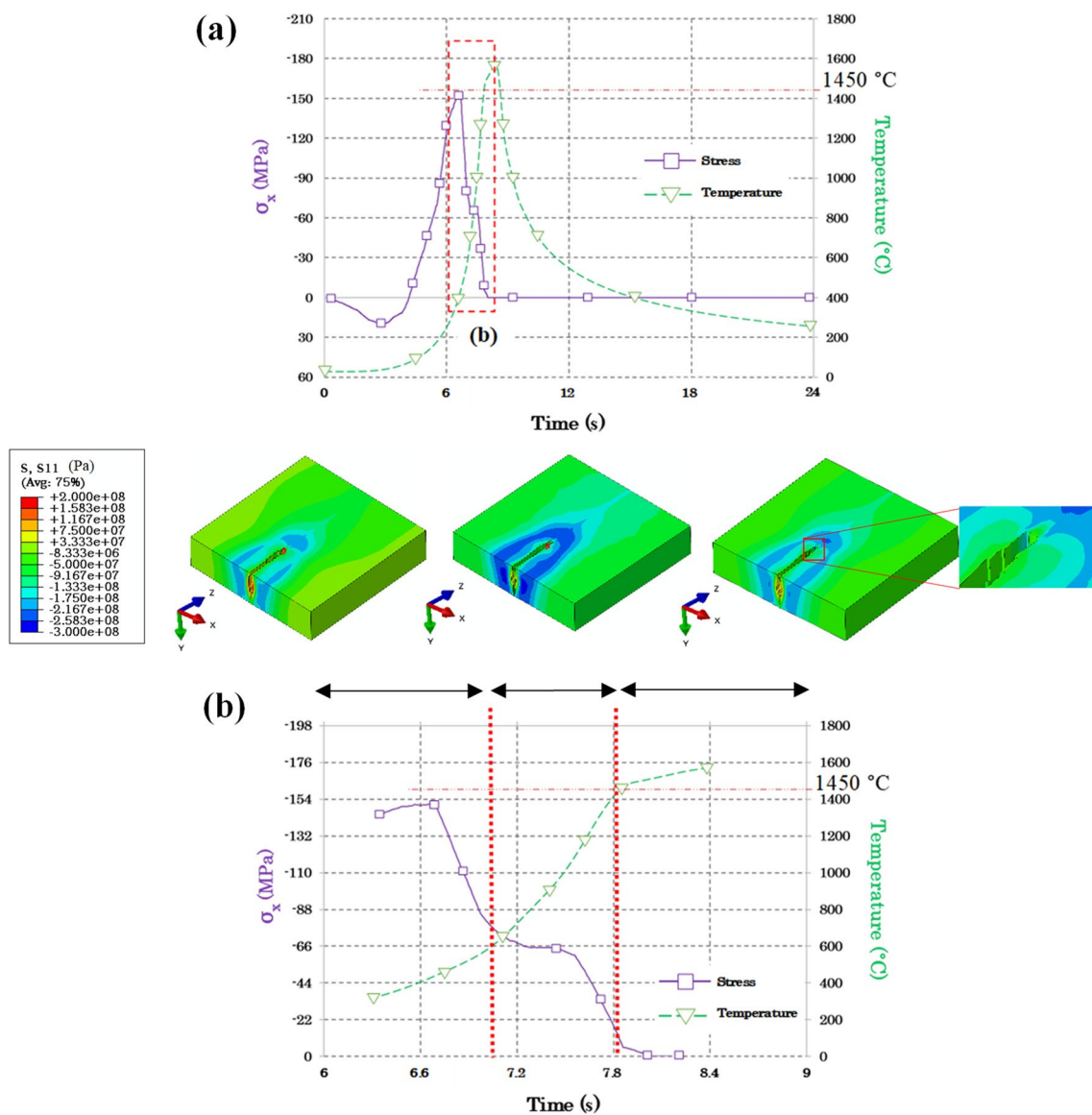


**Fig. 19** **a** Transverse stress ( $\sigma_x$ ) versus temperature history for an element on cutting line at  $z=0.5$  mm. **b** Magnified graph to see different steps of stress variation and element strength loss by increasing the temperature

tensile stress will increase, and therefore the stress state in the material will change from compressive to tensile. It is observed that the stress turns to zero when a ductile failure in noted, owing to stress concentration release upon plastic deformation and the element loses its total strength. It is confirmed by the material damage model explained in Eqs. (17) to (19).

Figure 19 represents the transverse stress  $\sigma_x$  versus temperature result at  $z=0.5$  mm. By approaching the laser at this location, the stress gradient becomes larger. This is induced by the presence of laser heat through conduction, which would yield a greater temperature gradient in the specimen.

Also, by laser movement through the cutting direction to this point, previous elements were removed from the cutting line due to a loss of strength. As shown in Fig. 19a, along the laser direction, the rise of local temperature increases the tensile stress of the element. As knowledge of fraction mechanics suggests, the maximum tension stress is located at the front of the crack [66]. Thereafter, the compressive stress increases significantly as the local temperature of the element reaches 600°C. The maximum difference at a fixed geometric point for stresses ranges from +20 MPa (at the start of the cutting process with a temperature below 200°C) to –151 MPa (at a temperature of 550°C just below

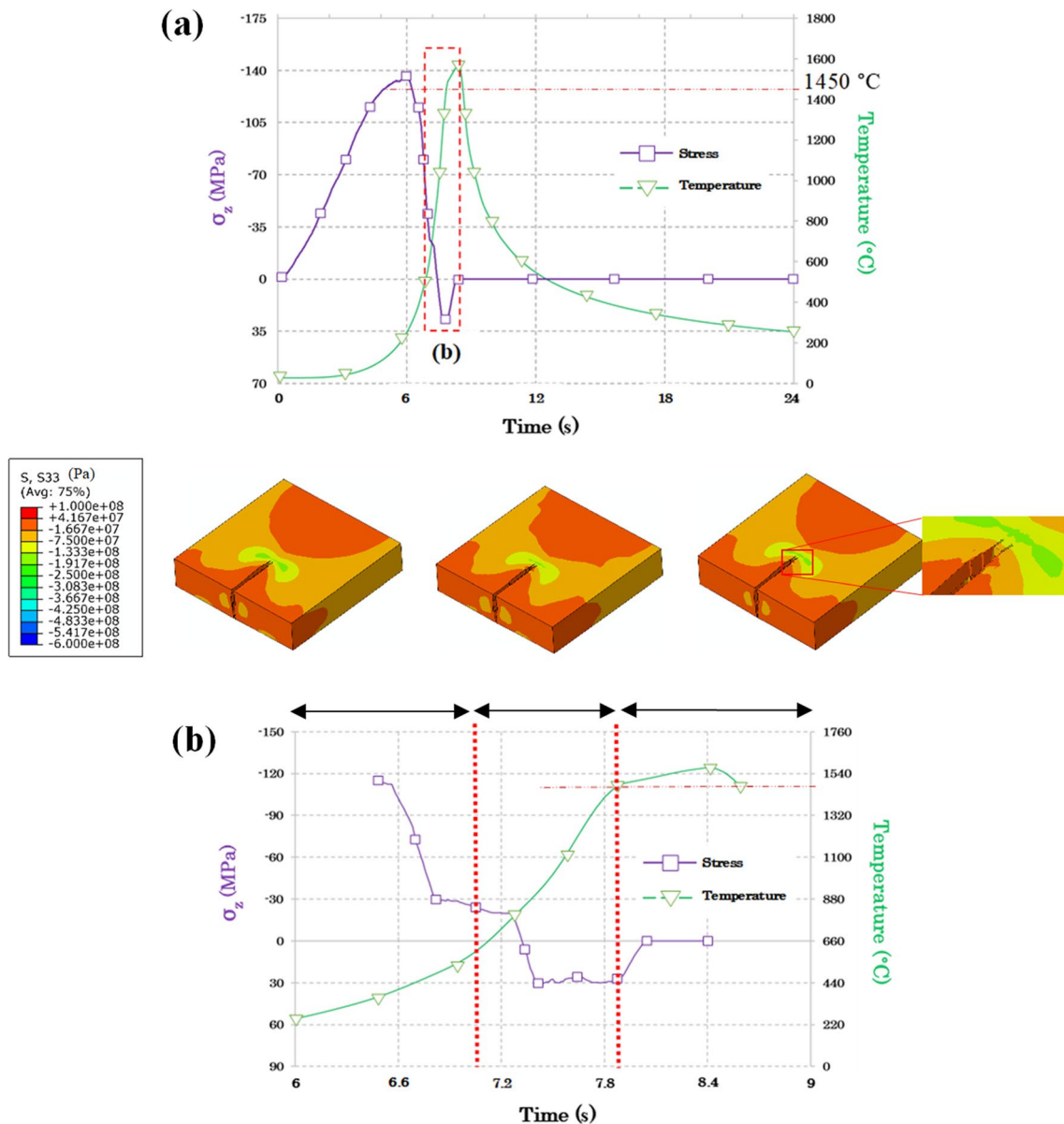


**Fig. 20** a Longitudinal stress ( $\sigma_z$ ) versus temperature history for an element on cutting line at  $z=0.5$  mm. b Magnified graph to see different steps of stress variation and element strength loss by increasing the temperature

the plastic strain point of 600°C of Si). A significant drop in stress is seen after the transition phase at 600°C, which entails a significant strength loss of the element, and the stress value turns to zero. As shown in Fig. 19b, a compressive stress zone in front of the tensile stress zone and on the sides can prevent the fracture front from transcending the laser spot irradiation zone, as discussed by other researchers [67, 68]. For regions with compression stresses, especially near the boundary, the stress decreases from the adjacent cutting surface to the exterior surface.

Figure 20 depicts the longitudinal stress  $\sigma_z$  versus temperature result at  $z=0.5$  mm. Figure 20a shows that when the laser spot is approaching the element at  $z=0.5$  mm, the Si wafer expands as the temperature rises gradually. This results in a great compressive longitudinal stress (139 MPa) at 200°C. Thereafter, the stress gradually decreases and even turns into tensile stress after the temperature passes 600°C. As the changes of the outer compared to the inner temperatures are more rapid, the differential dimensional changes cause restraint of the free changes, whether expansion or contraction of the volume adjacent to the Si wafer. Thus, rapid changes in temperature may lead to tensile stress.

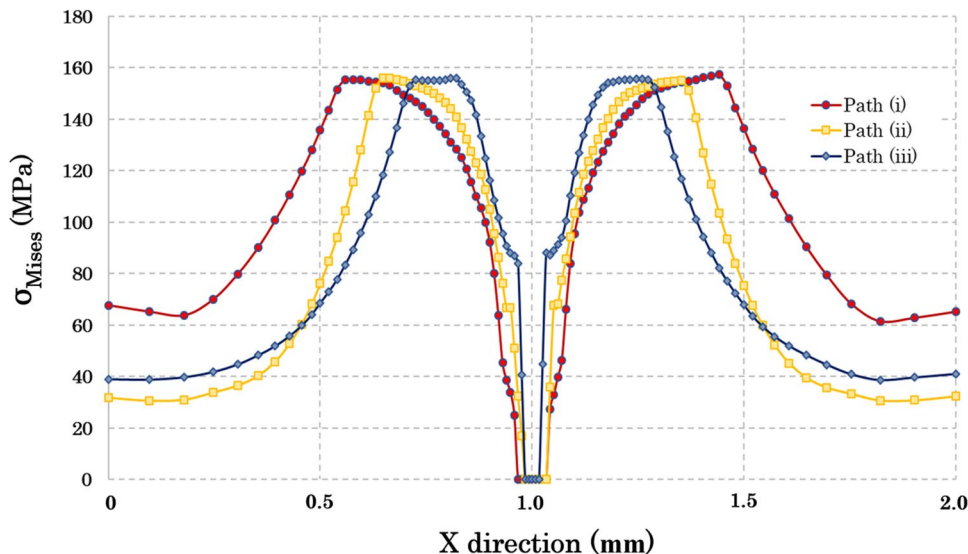
Figure 20b gives pictures and an enlarged view of the plotted graph within the time frame of element strength loss. The induced tensile nature of the stress, especially in the very neighbourhood of the cutting zone, will further accelerate damage and have a negative impact on the Si wafer in terms of its performance. The compressive nature of the stresses may have a slightly beneficial impact in terms of the mechanical properties and service life of Si, as discussed by Amer et al. [69].

The equivalent von Mises stress distribution is a prevalent method and commonly used yield criterion for forecasting material yield in engineering. This approach operates under the assumption that maximum deviatoric strain

energy triggers yielding in the material. For all simulations, the equivalent von Mises stress distribution provides a comprehensive analysis of the overall magnitude of these factors.

Figure 21 displays the von Mises stress through the thickness of the Si wafer, measured along three paths (shown in Fig. 16a). Numerical simulations show predominantly symmetric stress distributions, which are almost constant towards the specimen sides. Von Mises stress is more pronounced in areas with a significant temperature gradient, specifically in the vicinity of cutting edges. The anisotropic variation can be partly linked to the temperature profiles along the cutting direction (shown in Fig. 16b). At the centre of the model, the stress is equivalent to zero. Consequently, a loss of strength is seen, which is attributed to the lowering of the elastic modulus of the Si wafer due to temperature rise. Elements, with their temperatures having passed the melting point, lose their total strength and are subsequently removed from the region of cutting. A similar finding was shown in previous studies by Moradi et al. [63] and Fu et al. [70]. Whereas, a steep rise in the effective von Mises stress at the edges of the kerf is seen. This is attributed to showing higher strength by lowering temperature towards the boundary edges based on the temperature profile shown in Fig. 16b. Thereafter, minimum stress is seen along each path as it gradually decreases, resembling a similar pattern of temperature profile. Since path (i) is located on the top surface of the model, a larger area corresponds to zero stress due to excess heat energy accumulated by the laser, which confirms wider kerf width. After analysing the numerical outcome and experimental data, it was found that the variance in kerf width is less than 4  $\mu\text{m}$  and the deviation factor is below 5%. On the contrary, paths (ii) and (iii) are located at the middle and bottom surfaces through the material thickness, respectively. Through the stress analysis of the thickness of the model, one can identify von Mises stress gradients along

**Fig. 21** von Mises stress distribution for different paths along  $x$  direction at  $z=1$  mm



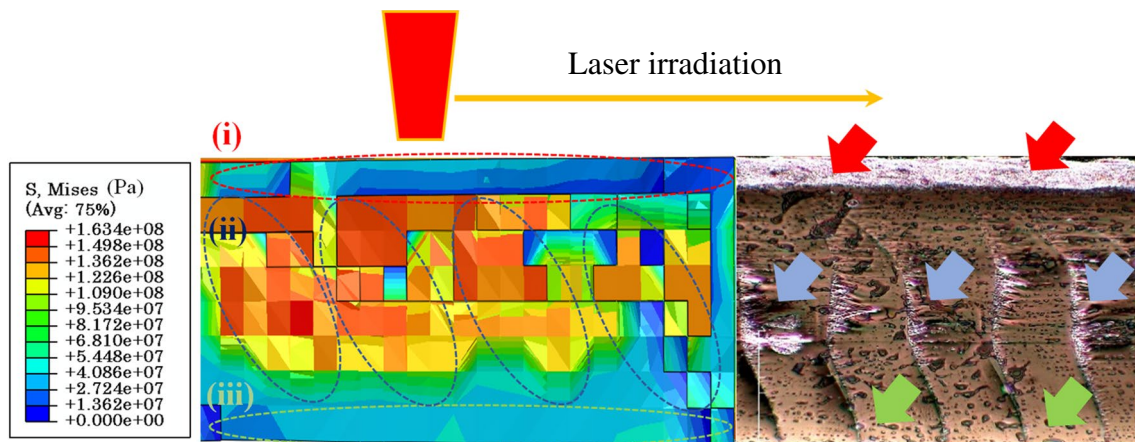


**Fig. 22** Side-by-side comparison of cutting cross-section between numerical simulation and experimental micrograph for specimen E1

paths (ii) and (iii), which reveal the degradation of elements owing to the heat conduction to the interior of the sample to create the whole cut. However, it is noted that increasing the rate of heat loss in the form of thermal convection and reducing the amount of heat entering the material through heat conduction cause a reduction in the amount of stress on the sides of the model. At position  $x=0.5$  or  $1.5$  mm along paths (ii) and (iii), there is a noteworthy reduction in stress levels to 60 MPa. Subsequently, there is a gradual decline in stress levels that remain consistent towards both ends.

Figure 22 shows a comparison of residual stresses for numerical and experimental results and their effect on the neighbourhood of the cutting zone with a relatively acceptable agreement. To facilitate comparison, the numerical outcome in Fig. 22 is partitioned into three distinct regions. It is seen that the area exposed to high laser heat (region (i)) is showing less stress values, which is attributed to a significant loss of strength at high temperature. This follows the same pattern in the experimental result, where the top part shown by the red arrow has completely burned and turned into solidified residues due to adverse thermal effects. On the contrary, by looking into the centre region of the Si thickness (region (ii)), the stress gradients show higher values up to 158 MPa. This result is confirmed by the blue arrows shown on the experimental micrograph, which indicates that the material on the surface of the cutting channel is ablated and some slags are adhered to on the cross-section of the cutting region. The bottom part, illustrated as region (iii), confirms minimum stress gradients and a roughly clear surface with no slags adhered to it. By looking at regions (i) to (iii), the degradation of the surface quality of the upper regions is due to the increased laser absorption at the wall with a reduction of the amount of delivered laser energy at the bottom of the zone due to several reflections from the wall, previously discussed by Soltani et al. [41]. The regular ripple-like step lines are seen on the fracture surfaces of the Si layer, which

represent the damage propagation and crack growth along the cutting line. Similar results were shown by Cai et al. [11], Zhao et al. [12], and Cheng et al. [13]. This is primarily due to the distribution of stress and related physical properties such as thermal expansion and thermal conductivity.

It is noted that the errors in the model arise primarily due to either the unavailability of reliable temperature-dependent properties or ignoring the presence of ambient atmosphere during laser absorption and flow within a molten pool or powder particle motion due to complexity.

## 5 Conclusion

This study presents the results and physics of a 350- $\mu\text{m}$ -thick semiconductor Si wafer processed using  $\text{CO}_2$  laser cutting both experimentally and numerically. Due to the highly reflective 10.6  $\mu\text{m}$   $\text{CO}_2$  laser, an increment of temperature was proposed to increase the material absorptivity locally. It was performed by decreasing the cutting speed at identical high laser power to enhance the absorptivity of Si. Unlike previous studies, this research considered a different modelling technique of Si wafer laser cutting. The sequentially coupled thermo-mechanical modelling was considered to calculate the thermal gradient and subsequently the stress distribution on the surface of the Si wafer. The BDT was employed to model the Si material behaviour at high temperatures, and therefore, Johnson–Cook plasticity and damage failure were concurrently defined to model the stress/failure mechanism. The main conclusions are drawn as follows:

- 1 The minimum value of cutting speed at high laser power and single laser pass (5 mm/min, 40 W, one laser pass) led to smaller kerf width, lesser HAZ, lower surface roughness, and good sidewall quality. On the other hand, considerable deposited residues and black spots induced

- by the laser beam were noted, especially at higher cutting speeds and with a higher number of passes.
- 2 A lower material removal rate was found as a result of laser ablation with a higher cutting speed, which is due to a slight reduction of laser efficiency. On the contrary, the increasing number of laser passes trapped a significant amount of laser heat and led to an increase in kerf width by melting and vaporising the silicon from the top surface.
  - 3 Highly extended HAZ was observed for both specimens E2 (10 mm/min and 3 laser passes) and E3 (20 mm/min and 6 laser passes) owing to significant heat conduction as a result of the temperature gradient in the workpiece. It concurs that the change of traversing speed impacts the time for interaction between the main stream and the cut, which may cause an incomplete first phase of cutting (complete penetration to the bottom surface of the material); therefore, increasing the number of passes and recoil pressure led to deteriorating the cutting quality.
  - 4 The analysis of EDX for specimen E1 showed that a significant amount of carbon material in the neighbourhood of the kerf edge was formed due to burning and highly induced heat from the laser; nevertheless, the distribution of silicon showed a high particle percentage (66.3%) for the selected region.
  - 5 In the numerical analysis, by moving the laser source energy along the cutting line, the elements were continuously heated, and they approached the melting temperature, which became a reason for a total loss of their strength and resulted in material failure. Temperature fields at selected reference cases showed consistent peaks and valleys in the time history curves. It was found that heat conduction plays a crucial role in rapid heat transfer to homogenise the temperature field. A temperature decay was observed through the thickness. On the other hand, upon the temperature variations at the specific heat capacity and thermal conductivity, the intensity of the temperature gradient decreased as the distance from the cutting line increased to the sides of the model perpendicularly, where a flat pattern was observed.
  - 6 The longitudinal and transverse stresses were plotted versus temperature gradients. Longitudinal stress is substantially lower than transverse stress due to thermal expansion and the direction of heat transfer. It was observed that rapid temperature changes at the top surface of silicon lead to rapid volume changes, which in turn cause tensile stress due to the constraining effect on adjacent volumes. However, the compressive stress near the area experiencing tension stopped the fracture from spreading beyond the zone where the laser was applied. It was also noted that Si experienced a phase change from an elastic behaviour to a complete plastic state

due to a laser heat increment. During the phase change, the material's physical properties, such as strength and stiffness, started degrading dramatically, resulting in an increment of the plastic strain rate.

- 7 For future experiments, it is recommended to explore the utilisation of higher-power CO<sub>2</sub> lasers across a spectrum of laser power settings and cutting speeds. This will enable an examination of the impact of increased input energy on the alterations in both the heat-affected zone and kerf properties. Additionally, conducting a comparative analysis of various numerical simulation models would provide valuable insights into stress gradients along the cutting perimeter.

**Supplementary Information** The online version contains supplementary material available at <https://doi.org/10.1007/s00170-024-13675-9>.

**Author contribution** Conceptualisation: Kaveh Moghadasi and Khairul Fikri Tamrin. Methodology: Kaveh Moghadasi and Khairul Fikri Tamrin. Software: Kaveh Moghadasi. Validation: Kaveh Moghadasi, Khairul Fikri Tamrin, and Nadeem Ahmed Sheikh. Formal analysis: Kaveh Moghadasi. Investigation: Kaveh Moghadasi, Khairul Fikri Tamrin, Nadeem Ahmed Sheikh, and Abdul Rahman Kram. Resources: Kaveh Moghadasi, Khairul Fikri Tamrin, and Pierre Barroy. Data curation: Kaveh Moghadasi, Khairul Fikri Tamrin, and Fahizan Mahmud. Writing—original draft preparation: Kaveh Moghadasi. Writing—review and editing: Khairul Fikri Tamrin, Nadeem Ahmed Sheikh, Pierre Barroy, and Amir Azam Khan. Visualisation: Kaveh Moghadasi. Supervision: Khairul Fikri Tamrin. Project administration: Khairul Fikri Tamrin. Funding acquisition: Khairul Fikri Tamrin. All authors have read and agreed to the published version of the manuscript.

**Funding** This study was funded by Universiti Malaysia Sarawak through Grant No. F02/PARTNERS/2107/2021 allocated to the project.

**Data availability** Not applicable.

**Code availability** Not applicable.

## Declarations

**Ethics approval** Not applicable.

**Consent to participate** Not applicable.

**Consent to publish** We would like to submit the enclosed manuscript, entitled “Experimental and Numerical Study of Thin Silicon Wafer Laser Cutting and Damage Investigation,” to The International Journal of Advanced Manufacturing Technology to be considered for publication. No conflict of interest exists in the submission of this manuscript, and the manuscript is approved by all authors for publication. We would like to declare on behalf of my co-authors that the work described is an original research that has not been published previously and is not under consideration for publication elsewhere, in whole or in part. All the authors listed have approved the manuscript that is enclosed.

**Conflict of interest** The authors declare no conflict of interest.

## References

- Atabaki AH, Moazeni S, Pavanello F, Gevorgyan H, Notaros J, Alloatti L, Wade MT, Sun C, Kruger SA, Meng H (2018) Integrating photonics with silicon nanoelectronics for the next generation of systems on a chip. *Nature* 556(7701):349–354
- Jiang Y, Li X, Liu B, Yi J, Fang Y, Shi F, Gao X, Sudzilovsky E, Parameswaran R, Koehler K (2018) Rational design of silicon structures for optically controlled multiscale biointerfaces. *Nat Biomed Eng* 2(7):508–521
- Arif M, Rahman M, San WY (2012) A state-of-the-art review of ductile cutting of silicon wafers for semiconductor and microelectronics industries. *Int J Adv Manuf Technol* 63:481–504
- Li Z, Allegra O, Li Q, Guo W, Li L (2021) Femtosecond laser single step, full depth cutting of thick silicon sheets with low surface roughness. *Opt Laser Technol* 138:106899
- Mottay E, Liu X, Zhang H, Mazur E, Sanatinia R, Pflieger W (2016) Industrial applications of ultrafast laser processing. *MRS Bull* 41(12):984–992
- Domke M, Egle B, Piredda G, Fasching G, Bodea M, Schwarz E (2015) Controlling depth and distance of the hole formations at the bottom of laser-scribed trenches in silicon using fspulses. In *Laser Applications in Microelectronic and Optoelectronic Manufacturing (LAMOM) XX*. SPIE 9350:177–182
- Fang Z, Chen L, Guan Y, Zheng H (2020) Picosecond laser micromachining of silicon wafer: characterizations and electrical properties. *Surf Rev Lett* 27(05):1950142
- Neuenschwander B, Jaeggi B, Foerster DJ, Kramer T, Remund S (2019) Influence of the burst mode onto the specific removal rate for metals and semiconductors. *J Laser Appl* 31(2):022203
- Metzner D, Lickschat P, Weißmantel S (2019) Laser micromachining of silicon and cemented tungsten carbide using picosecond laser pulses in burst mode: ablation mechanisms and heat accumulation. *Appl Phys A* 125(7):1–8
- Shaheen ME, Gagnon JE, Fryer BJ (2019) Studies on laser ablation of silicon using near IR picosecond and deep UV nanosecond lasers. *Opt Lasers Eng* 119:18–25
- Cai Y, Yang L, Zhang H, Wang Y (2016) Laser cutting silicon-glass double layer wafer with laser induced thermal-crack propagation. *Opt Lasers Eng* 82:173–185
- Zhao C, Cai Y, Ding Ye, Yang L, Wang Z, Wang Y (2020) Investigation on the crack fracture mode and edge quality in laser dicing of glass-anisotropic silicon double-layer wafer. *J Mater Process Technol* 275:116356
- Cheng X, Yang L, Wang M, Cai Y, Wang Y, Ren Z (2019) Laser beam induced thermal-crack propagation for asymmetric linear cutting of silicon wafer. *Opt Laser Technol* 120:105765
- Cheng X, Yang L, Wang M, Cai Y, Wang Y, Ren Z (2019) The unbiased propagation mechanism in laser cutting silicon wafer with laser induced thermal-crack propagation. *Appl Phys A* 125(7):1–11
- Wang H-J, Yang T (2021) A review on laser drilling and cutting of silicon. *J Eur Ceram Soc* 41(10):4997–5015
- Witteman WJ (2013) *The CO2 laser*. Vol. 53. Springer
- Venkatakrishnan K, Tan Bo (2007) Thin silicon wafer dicing with a dual-focused laser beam. *J Micromech Microeng* 17(12):2505
- Daud ND, Hasan MN, Saleh T, Leow PL, Ali MSM (2022) Non-traditional machining techniques for silicon wafers. *Int J Adv Manuf Technol* 121(1–2):29–57
- Tangwarodomnukun V, Wang J, Huang CZ, Zhu HT (2012) An investigation of hybrid laser–waterjet ablation of silicon substrates. *Int J Mach Tools Manuf* 56:39–49
- Huang Y-F, Chattopadhyay S, Jen Y-J, Peng C-Y, Liu T-A, Hsu Y-K, Pan C-L, Lo H-C, Hsu C-H, Chang Y-H (2007) Improved broadband and quasi-omnidirectional anti-reflection properties with biomimetic silicon nanostructures. *Nat Nanotechnol* 2(12):770–774
- Chichkov BN, Momma C, Nolte S, Von Alvensleben F, Tünnermann A (1996) Femtosecond, picosecond and nanosecond laser ablation of solids. *Appl Phys A* 63(2):109–115
- Esmail I, YazdaniSarvestani H, Gholipour J, Ashrafi B (2021) Engineered net shaping of alumina ceramics using picosecond laser. *Optics Laser Technol* 135:106669
- Guo Y, Haijun S, Zhou H, Shen Z, Liu Y, Zhang J, Liu L, Hengzhi F (2022) Unique strength-ductility balance of AlCoCrFeNi<sub>2</sub>. 1 eutectic high entropy alloy with ultra-fine duplex microstructure prepared by selective laser melting. *J Mater Sci Technol* 111:298–306
- Esmailizadeh R, Keshavarzkermani A, Ali U, Mahmoodkhani Y, Behraves H, Jahed H, Bonakdar A, Toyserkani E (2020) Customizing mechanical properties of additively manufactured Hastelloy X parts by adjusting laser scanning speed. *J Alloy Compd* 812:152097
- Liu SY, Li HQ, Qin CX, Zong R, Fang XY (2020) The effect of energy density on texture and mechanical anisotropy in selective laser melted Inconel 718. *Mater Des* 191:108642
- Zhenhua Lei, Yubin Zhang, Qingzhi Li, Ting Shao, Laixi Sun, Kaixuan Wang, Zao Yi, Xin Ye, Wanguo Zheng, and Pinghui Wu (2022) Numerical and experimental study on thermal damage induced by medium—infrared laser. *Photonics*. MDPI
- Boyd IW, Binnie TD, Wilson JIB, Colles MJ (1984) Absorption of infrared radiation in silicon. *J Appl Phys* 55(8):3061–3063
- Shangguan Q, Chen Z, Yang H, Cheng S, Yang W, Yi Z, Xianwen Wu, Wang S, Yi Y, Pinghui Wu (2022) Design of ultra-narrow band graphene refractive index sensor. *Sensors* 22(17):6483
- Sehyeok Oh, Lee I, Park Y-B, Ki H (2019) Investigation of cut quality in fiber laser cutting of CFRP. *Opt Laser Technol* 113:129–140
- Li M, Li S, Yang X, Zhang Yi, Liang Z (2018) Fiber laser cutting of CFRP laminates with single-and multi-pass strategy: a feasibility study. *Opt Laser Technol* 107:443–453
- Moghadasi K, Tamrin KF (2020) Experimental investigation and parameter optimization of low power CO<sub>2</sub> laser cutting of a carbon/Kevlar fiber-reinforced hybrid composite. *Lasers Eng (Old City Publ)* 45(1–3):85–108
- Leone C, Genna S, Tagliaferri V (2014) Fibre laser cutting of CFRP thin sheets by multi-passes scan technique. *Opt Lasers Eng* 53:43–50
- Tamrin KF, Moghadasi K, Jalil MH, Sheikh NA, Mohamaddan S (2021) Laser discoloration in acrylic painting of visual art: experiment and modeling. *Materials* 14(8):2009
- Shaikh AA, Azharuddin AMD, Anjum A (2023) Comparative assessment of experimental and numerical simulation of ablation depth in PMMA multipass laser cutting. *Acta Technica Napocensis-Ser: Appl Math, Mech, Eng* 65:4S
- Sotnikov A, Laux H, Stritzker B (2010) Experimental and numerical optimization of beam shapes for short-pulse ultraviolet laser cutting processing. *Phys Procedia* 5:137–146
- James M Bovatsek and Rajesh S Patel (2010) Highest-speed dicing of thin silicon wafers with nanosecond-pulse 355nm q-switched laser source using line-focus fluence optimization technique. *Laser-based Micro-and Nanopackaging and Assembly IV*. SPIE
- Anjum A, Shaikh AA, Tiwari N (2023) Comparative assessment of the developed algorithm with the soft computing algorithm for the laser machined depth. *Infrared Phys Technol* 129:104545
- Subramonian S, Kasim MS, Mohd Amran Md, Ali RI, Abdullah R, Anand T (2015) Micro-drilling of silicon wafer by industrial CO<sub>2</sub> laser. *Int J Mech Mater Eng* 10(1):1–6

39. Balbaa M, Mekhail S, Elbestawi M, McIsaac J (2020) On selective laser melting of Inconel 718: densification, surface roughness, and residual stresses. *Mater Des* 193:108818
40. Richter B, Blanke N, Werner C, Parab ND, Sun T, Vollertsen F, Pfefferkorn FE (2019) High-speed X-ray investigation of melt dynamics during continuous-wave laser remelting of selective laser melted Co-Cr alloy. *CIRP Annals* 68(1):229–232
41. Soltani B, Azarhoushang B, Zahedi A (2019) Laser ablation mechanism of silicon nitride with nanosecond and picosecond lasers. *Opt Laser Technol* 119:105644
42. Yeo CY, Tam SC, Jana S, Lau MWS (1994) A technical review of the laser drilling of aerospace materials. *J Mater Proc Technol* 42(1):15–49
43. Kononenko TV, Freitag C, Komlenok MS, Weber R, Graf T, Konov VI (2018) Heat accumulation between scans during multi-pass cutting of carbon fiber reinforced plastics. *Appl Phys A* 124(2):217
44. Anjum A, Shaikh AA, Tiwari N (2022) Experimental investigations of channel profile and surface roughness on PMMA substrate for microfluidic devices with mathematical modelling. *Optik* 261:169154
45. Ganeev RA (2018) Nanostructured nonlinear optical materials: formation and characterization. Elsevier, pp 1–410
46. Micallef C, Zhuk Y, Aria AI (2020) Recent progress in precision machining and surface finishing of tungsten carbide hard composite coatings. *Coatings* 10(8):731
47. Liu Y, Zhang S, Zhao Y, Ren Z (2022) Experiments on the kerf quality characteristic of mild steel while cutting with a high-power fiber laser. *Opt Laser Technol* 154:108332
48. Mustafa AY (2018) Modelling of the hole quality characteristics by extreme learning machine in fiber laser drilling of Ti-6Al-4V. *J Manuf Process* 36:138–148
49. Osipov AV, Patzner P, Hess P (2006) Kinetics of laser-induced oxidation of silicon near room temperature. *Appl Phys A* 82:275–280
50. Ma Y, Si J, Sun X, Chen T, Hou X (2014) Progressive evolution of silicon surface microstructures via femtosecond laser irradiation in ambient air. *Appl Surf Sci* 313:905–910
51. Sharif Uddin M, Seah KHW, Rahman M, Li XP, Liu K (2007) Performance of single crystal diamond tools in ductile mode cutting of silicon. *J Mater Proc Technol* 185(1–3):24–30
52. Moghadasi K, Tamrin KF, Sheikh NA, Jawaid M (2021) A numerical failure analysis of laser micromachining in various thermoplastics. *Int J Adv Manuf Technol* 117(1):523–538
53. Moghadasi K, Tamrin KF (2020) Multi-pass laser cutting of carbon/Kevlar hybrid composite: Prediction of thermal stress, heat-affected zone, and kerf width by thermo-mechanical modeling. *Proc Inst Mech Eng, Part L: J Mater: Des Appl* 234(9):1228–1241
54. Sturm JC, Reaves CM (1992) Silicon temperature measurement by infrared absorption. Fundamental processes and doping effects. *IEEE Trans Electron Devices* 39(1):81–88
55. Masolin A, Bouchard P-O, Martini R, Bernacki M (2013) Thermo-mechanical and fracture properties in single-crystal silicon. *J Mater Sci* 48:979–988
56. Tilli M, Paulasto-Kröckel M, Petzold M, Theuss H, Motooka T, Lindroos V (eds) (2020) Handbook of silicon based MEMS materials and technologies. Elsevier, pp 1–984
57. Green MA (2008) Self-consistent optical parameters of intrinsic silicon at 300 K including temperature coefficients. *Solar Energy Mater Solar Cells* 92(11):1305–1310
58. Okada Y, Tokumaru Y (1984) Precise determination of lattice parameter and thermal expansion coefficient of silicon between 300 and 1500 K. *J Appl Phys* 56(2):314–320
59. Yan J, Zhao H, Kuriyagawa T (2009) Effects of tool edge radius on ductile machining of silicon: an investigation by FEM. *Semicond Sci Technol* 24(7):075018
60. Han C-F, Lin C-C, Lin J-F (2021) Applications of energy flux and numerical analyses to the plasma etching of silicon deep trench isolation (DTI) structures. *Precis Eng* 71:141–152
61. Han C-F, Lin J-F (2016) Thermally-induced failures of copper through-silicon via structures evaluated by the strain energy density model. *Thin Solid Films* 615:281–291
62. Yilbas BS, Akhtar SS, Karatas C (2017) Laser circular cutting of Kevlar sheets: analysis of thermal stress field and assessment of cutting geometry. *Opt Laser Technol* 96:180–189
63. Moradi M, Moghadam MK, Shamsborhan M, Beiranvand ZM, Rasouli A, Vahdati M, Bakhtiari A, Bodaghi M (2021) Simulation, statistical modeling, and optimization of CO<sub>2</sub> laser cutting process of polycarbonate sheets. *Optik* 225:164932
64. Anjum A, Shaikh A (2023) Experimental and analytical modeling for channel profile using CO<sub>2</sub> laser considering gaussian beam distribution. *J Eng Re* 11(2):100035
65. Noori Rahim Abadi SMA, Mi Y, Sikström F, Ancona A, Choquet I (2021) Effect of shaped laser beam profiles on melt flow dynamics in conduction mode welding. *Int J Thermal Sci* 166:106957
66. Lawn B (1993) Fracture of brittle solids. Cambridge University Press, pp 1–371
67. Liu T, Ge P, Bi W, Gao Y (2017) Subsurface crack damage in silicon wafers induced by resin bonded diamond wire sawing. *Mater Sci Semicond Process* 57:147–156
68. Anjum A, Shaikh AA, Tiwari N (2023) Experimental investigations and modeling for multi-pass laser micro-milling by soft computing-physics informed machine learning on PMMA sheet using CO<sub>2</sub> laser. *Optics Laser Technol* 158:108922
69. Amer MS, Dosser L, LeClair S, Maguire JF (2002) Induced stresses and structural changes in silicon wafers as a result of laser micro-machining. *Appl Surf Sci* 187(3–4):291–296
70. Fu CH, Sealy MP, Guo YB, Wei XT (2015) Finite element simulation and experimental validation of pulsed laser cutting of nitinol. *J Manuf Proc* 19:81–86

**Publisher's Note** Springer Nature remains neutral with regard to jurisdictional claims in published maps and institutional affiliations.

Springer Nature or its licensor (e.g. a society or other partner) holds exclusive rights to this article under a publishing agreement with the author(s) or other rightsholder(s); author self-archiving of the accepted manuscript version of this article is solely governed by the terms of such publishing agreement and applicable law.